Energy Materials and Devices

Open Access
Review

Graphical Abstract

Eco-friendly lead-free and low-lead perovskite solar cells

Changkai Huang[1], Yihuai Huang[1], Qiannan Zhao[1], Zhenxuan Liu[1], Guibin Shen[3] ✉, Qinghui Jiang[1], Yubo Luo[1], Xin Li[1,2] ✉, and Junyou Yang[1] ✉

[1] *State Key Laboratory of Materials Processing and Die & Mould Technology, School of Materials Science and Engineering, Huazhong University of Science and Technology, Wuhan 430074, China*
[2] *Guangdong HUST Industrial Technology Research Institute, Guangdong Provincial Key Laboratory of Manufacturing Equipment Digitization, Dongguan 523808, China*
[3] *School of Electrical and Electronic Engineering, Nanyang Technological University, Singapore 639798, Singapore*

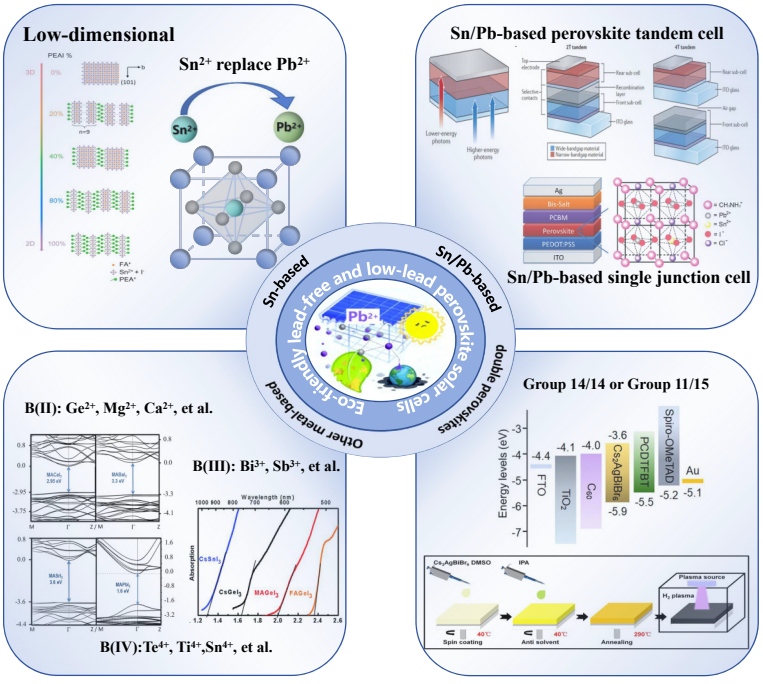

This review presents a comprehensive overview of recent advancements in eco-friendly lead-free and low-lead perovskite solar cells. It covers a range of systems, including Sn-based (organic–inorganic hybrid, low-dimensional, and all-inorganic), Sn–Pb-based (single-junction and tandem), other metal-based (Ge, Bi, Sb, etc.), and double perovskite materials. The discussion emphasizes material design, device performance, stability, and optimization strategies, while also highlighting the limitations and future prospects of these perovskite systems.

✉Address correspondence to
Guibin Shen, guibin.shen@ntu.edu.sg;
Xin Li, xin_li@hust.edu.cn;
Junyou Yang, jyyang@mail.hust.edu.cn

Received: December 16, 2025
Revised: February 20, 2026
Accepted: March 9, 2026

9370089

Read Online

Citation: Huang C., Huang Y., Zhao Q., et al. Eco-friendly lead-free and low-lead perovskite solar cells. *Energy Mater. Devices*, 2026, 4(1), 9370089. https://doi.org/10.26599/EMD.2026.9370089

Energy Materials and Devices
https://doi.org/10.26599/EMD.2026.9370089
Open Access
Review

Eco-friendly lead-free and low-lead perovskite solar cells

Changkai Huang[1], Yihuai Huang[1], Qiannan Zhao[1], Zhenxuan Liu[1], Guibin Shen[3] ✉, Qinghui Jiang[1], Yubo Luo[1], Xin Li[1,2] ✉, and Junyou Yang[1] ✉

[1] *State Key Laboratory of Materials Processing and Die & Mould Technology, School of Materials Science and Engineering, Huazhong University of Science and Technology, Wuhan 430074, China*
[2] *Guangdong HUST Industrial Technology Research Institute, Guangdong Provincial Key Laboratory of Manufacturing Equipment Digitization, Dongguan 523808, China*
[3] *School of Electrical and Electronic Engineering, Nanyang Technological University, Singapore 639798, Singapore*

Cite this article: *Energy Mater. Devices* 2026, **4**(1): 9370089. https://doi.org/10.26599/EMD.2026.9370089

ABSTRACT

Perovskite solar cells (PSCs) have attracted significant attention due to their rapid improvements in power conversion efficiency (PCE). However, the environmental hazards of lead-containing perovskites have intensified the need for lead-free alternatives. This review summarizes recent advances in lead-free and low-lead PSCs, focusing on material design, performance optimization, and stability enhancement. We first examine tin (Sn)-based perovskites, the most extensively studied lead-free system. Despite achieving PCEs up to 18%, their practical deployment is limited by Sn^{2+} oxidation, high background carrier density, and restricted long-term stability. Tin-lead (Sn–Pb) mixed perovskites are then discussed as a low-lead strategy that balances environmental safety with high performance, achieving certified efficiencies exceeding 24% for single-junction cells and over 28% in tandem devices. Other metal-based and double perovskites are also reviewed, with attention to their electronic structure limitations and potential optimization strategies. Finally, we highlight the key challenges and future directions. Commercialization remains constrained by issues including material stability, bandgap tuning, and scalable fabrication. This review provides a comprehensive framework for guiding the development of efficient, stable, and environmentally benign lead-free PSCs.

KEYWORDS

lead-free perovskite solar cells, Sn-based perovskites, bandgap tuning, compositional regulation

1 Introduction

Amid the global push for sustainable energy solutions, solar energy has gained significant attention as a clean and renewable resource. Since the first report of organic–inorganic hybrid perovskite solar cells (PSCs) in 2009[1], their rapid improvements in power conversion efficiency (PCE) have placed them at the forefront of photovoltaic research. Over the past decade, PCE has increased from 3.8% to over 26%, highlighting their strong potential for practical applications that may rival conventional silicon-based solar cells[2,3]. Perovskite materials generally follow the ABX_3 formula, where A represents an organic or alkali metal cation (e.g., $CH_3NH_3^+$ (MA^+), $HC(NH_2)_2^+$ (FA^+), or Cs^+), B is a divalent metal cation (e.g., Pb^{2+}, Sn^{2+}, or Ge^{2+}), and X is a halide anion (e.g., Cl^-, Br^-, or I^-)[4]. In this structure, the A, B, and X ions must satisfy the tolerance factor t[5], typically ranging from 0.813 to 1.107, defined $t = (r_A + r_X)/\sqrt{2}(r_B + r_X)$, where r_A, r_B, and r_X denote the ionic radii of A, B, and X, respectively. PSCs commonly rely on lead (Pb)-based perovskites such as $CH_3NH_3PbI_3$[6–8]. However, the widespread use of lead raises serious environmental concerns throughout the device lifecycle. Lead leakage can contaminate soil and water systems, posing risks to ecosystems and human health[9].

The preceding discussion highlights the urgent need to develop environmentally friendly lead-free or low-lead PSCs. These materials provide a promising approach to addressing current challenges owing to their structural diversity. For example, tin (Sn)-based perovskites such as $CsSnI_3$ and $MASnI_3$ exhibit crystal structures similar to those of their Pb-based counterparts[10–12] and possess theoretically favorable optoelectronic properties. The smaller ionic radius of Cs^+ contributes to lattice stabilization, thereby improving the structural stability of Sn-based perovskites to some extent[12,13]. Furthermore, bandgap tuning through halide ion substitution enables optimization of light absorption under different illumination conditions. For instance, introducing Br^- ions into $CH_3NH_3SnI_3$ increases the bandgap from approximately 1.3 eV to about 2.15 eV, which can improve PCE by adjusting the absorption range within the visible spectrum[11]. However, despite their promising theoretical optoelectronic properties, pure Sn-based perovskites

Received: December 16, 2025 / **Revised:** February 20, 2026 / **Accepted:** March 9, 2026

✉**Address correspondence to** Guibin Shen, guibin.shen@ntu.edu.sg; Xin Li, xin_li@hust.edu.cn; Junyou Yang, jyyang@mail.hust.edu.cn

exhibit poor stability and limited charge-carrier mobility, which hinder their practical application. Compared with fully lead-free perovskites, controlled lead incorporation (i.e., low-lead perovskites) has been shown to effectively mitigate these limitations. In particular, Sn–Pb alloyed perovskites exhibit strong potential for commercialization. The introduction of an appropriate amount of lead can partially compensate for the poor stability and low carrier mobility of pure Sn-based perovskites[14]. Moreover, optimization of the Sn/Pb composition ratio can enhance PCE while reducing environmental concerns associated with high lead content[15]. In this context, Sn–Pb PSCs have achieved power conversion efficiencies exceeding 20% and demonstrated significantly improved stability through precise tuning of the Sn/Pb ratio, together with interface engineering and quantum dot doping. For example, one study reported that encapsulated devices retained 90% of their initial efficiency after 795 h under simulated one-sun illumination[16], providing strong support for their potential industrial scalability.

Other metal-based perovskites also offer distinct advantages. For example, Bi-based perovskites such as $Cs_3Bi_2I_9$ exhibit excellent air stability and strong resistance to degradation under humid conditions[17], making them promising candidates for long-term outdoor applications without complex encapsulation. In addition, recent first-principles studies have examined a series of $Cs_2BB'X_6$ double perovskites and explored their potential as lead-free photovoltaic materials with favorable optoelectronic properties[18]. These materials exhibit tunable bandgaps spanning the visible to near-infrared regions and relatively low charge-carrier effective masses, which support efficient charge transport and extraction.

Several previous reviews have examined specific aspects of lead-free PSCs, often focusing on particular material families such as Sn-based or double perovskites. However, a comprehensive comparative analysis covering the full spectrum of lead-free and low-lead systems, including Sn-based, Sn–Pb hybrid, other metal-based, and double perovskites, remains limited. This review summarizes the development of these systems, discusses current research bottlenecks, and highlights prospective directions with realistic potential for large-scale commercialization. The following sections review recent progress in lead-free PSCs, with emphasis on Sn-based and Sn–Pb alloyed perovskites, while briefly discussing other metal-based and double perovskite systems in the final section.

2 Sn-based PSCs

Sn-based PSCs have emerged as a promising research direction within the field of lead-free perovskites and have attracted increasing attention in recent years. These materials share the same general chemical formula, ABX_3[10], as their Pb-based counterparts. Owing to their unique material properties, Sn-based perovskites provide a potential strategy to mitigate the environmental concerns associated with conventional lead-containing PSCs. In addition, organic–inorganic hybrid perovskites, low-dimensional Sn halide perovskites, and all-inorganic Sn halide perovskites exhibit diverse structural forms and offer several advantages that have attracted significant research interest worldwide. This section presents an overview of recent advances in Sn-based PSCs.

2.1 Sn-based organic–inorganic hybrid perovskite

Sn-based organic–inorganic hybrid perovskites represent a major class of materials in lead-free PSCs, in which the A-site is occupied by organic cations and the B-site is occupied by Sn^{2+} ions. In 2014, Noel et al. reported the first fully lead-free $CH_3NH_3SnI_3$ perovskite solar cell, achieving a maximum PCE of 6.4% by spin-coating the perovskite precursor solution onto a mesoporous TiO_2 layer[10]. $CH_3NH_3SnI_3$ adopts a tetragonal crystal phase similar to that of the widely studied $CH_3NH_3PbX_3$ perovskites (Fig. 1a), indicating that substitution of the central metal cation does not significantly alter the overall perovskite crystal framework. However, these materials still suffer from short charge-carrier diffusion lengths and poor stability, highlighting the need for further improvement. Similarly, Hao et al. introduced Br^- ions to partially substitute I^- in $CH_3NH_3SnI_3$, producing a series of $CH_3NH_3SnI_{3-x}Br_x$ (x = 0, 1, 2, 3) perovskites with tunable bandgaps[11]. Figure 1b shows a representative cross-sectional scanning electron microscopy (SEM) image of a typical solar cell device. As shown in Fig. 1c, the absorption onset of $CH_3NH_3SnI_{3-x}Br_x$ shifts from 954 nm (1.30 eV for $CH_3NH_3SnI_3$) to 577 nm (2.15 eV for $CH_3NH_3SnBr_3$), demonstrating significant tunability of the optical properties of these perovskite photovoltaic materials (illustrated in the right panel of Fig. 1b). The intermediate mixed-halide perovskites $CH_3NH_3SnI_2Br$ and $CH_3NH_3SnIBr_2$ exhibit absorption onsets at 795 nm (1.56 eV) and 708 nm (1.75 eV), respectively.

The band alignment diagram indicates an increase in the bandgap (E_g) of $CH_3NH_3SnI_{3-x}Br_x$ compounds, which is attributed to an upward shift of the conduction band with increasing Br/I ratio, while the valence band remains nearly unchanged (Fig. 1d). This bandgap widening leads to a higher open-circuit voltage (V_{oc}) but a lower short-circuit current density (J_{sc}). Notably, the device based on $CH_3NH_3SnIBr_2$ achieved the highest PCE of 5.73%[11]. In addition, solvent evaporation can adversely affect the formation of uniform, pinhole-free $MASnI_3$ perovskite films. Rapid solvent evaporation promotes the formation of SnI_2 and methylammonium iodide (MAI) precursor phases during film formation, which differs from the crystallization behavior observed in the $MAPbI_3$ system[19]. This observation highlights the critical role of solvent engineering in improving film quality. Four commonly used high-polarity solvents—dimethyl sulfoxide (DMSO), *N*,*N*-dimethylformamide (DMF), *N*-methyl-2-pyrrolidone (NMP), and γ-butyrolactone (GBL)—strongly influence the crystallization behavior of $MASnI_3$ perovskite films primarily through their Lewis base coordination with Sn^{2+} and the resulting halide complexes. For example, DMSO stabilizes the intermediate SnI_2·3DMSO phase and facilitates the formation of highly uniform, pinhole-free $CH_3NH_3SnI_3$ films, resulting in a record photocurrent density of up to 21 mA cm^{-2} (Fig. 1e)[19]. Weiss et al. employed a two-step fabrication process for $CH_3NH_3SnI_3$ light-absorbing layers, in which a tin iodide (SnI_2) layer deposited by physical vapor deposition reacts with a spin-coated MAI solution[20]. The resulting films exhibited

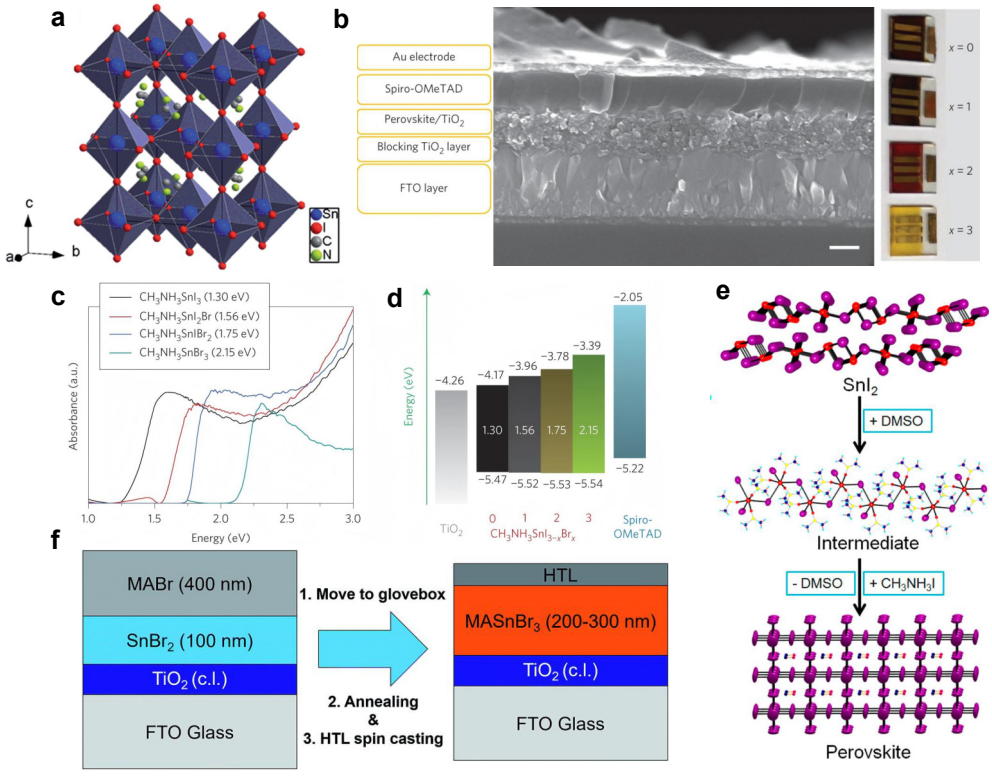

Figure 1 (a) Crystal structure of $CH_3NH_3SnI_3$. Reproduced with permission from Ref. [10] ©2014, The Royal Society of Chemistry. (b) Representative cross-sectional SEM image of a completed photovoltaic device based on $CH_3NH_3SnI_3$. (c) Absorption spectra of $CH_3NH_3SnI_{3-x}Br_x$ perovskites. (d) Energy-level diagram of $CH_3NH_3SnI_{3-x}Br_x$ with TiO_2 and spiro-OMeTAD as the hole-transporting material. Reproduced with permission from Ref. [11] ©2014, Springer Nature Limited. (e) Schematic illustration of $CH_3NH_3SnI_3$ perovskite film formation from SnI_2 via the SnI_2·3DMSO intermediate. Reproduced with permission from Ref. [19] ©2015, American Chemical Society. (f) Schematic of the sequential evaporation fabrication process. Reproduced under the CC BY-NC 3.0 license from Ref. [21] ©2016, The Royal Society of Chemistry.

complete surface coverage, with tin predominantly in the Sn^{2+} oxidation state, and showed improved environmental stability. These results indicate that vapor-phase deposition is a promising approach for producing uniform and compact $CH_3NH_3SnI_3$ films. Similarly, Jung et al. fabricated planar $MASnBr_3$ PSCs using both co-evaporation and sequential evaporation methods, achieving power conversion efficiencies of 0.35% and 1.12%, respectively (Fig. 1f)[21]. Among the materials reported in the aforementioned studies, $CH_3NH_3SnI_3$ demonstrated the best device performance, achieving a maximum PCE of 6.4%, higher than that of $CH_3NH_3SnIBr_2$ (5.73%) and $CH_3NH_3SnBr_3$ (less than 2%). When combined with DMSO-based solvent engineering, the photocurrent density reached up to 21 mA cm^{-2}, indicating promising practical potential. Although mixed-halide variants offer tunable optical properties, their current efficiency trade-offs make them less competitive than $CH_3NH_3SnI_3$.

When the smaller methylammonium cation (MA^+) in $MASnI_3$ is replaced by the larger formamidinium cation (FA^+), the resulting $FASnI_3$ material exhibits a bandgap of 1.41 eV (Fig. 2a), which is slightly larger than that of $MASnI_3$ and slightly smaller than that of $FAPbI_3$ (1.47 eV)[23]. Experimental studies by Dang et al. reported that $FASnI_3$ possesses a remarkably low trap density (~10^{11} cm^{-3})[24], which contributes to improved resistance to moisture and oxygen and thus enhances ambient stability compared with $MASnI_3$[24,25]. Koh et al. reported the first $FASnI_3$-based solar cell incorporating SnF_2, achieving a PCE of 2.1%[22]. X-ray photoelectron spectroscopy (XPS) analysis indicated the presence of only Sn^{2+}, with no detectable Sn^{4+} signal. This result suggests that the Sn in the perovskite films remained predominantly in the unoxidized Sn^{2+} state, which is beneficial for device performance (Fig. 2b). An additional observation was that the color of the $FASnI_3$ precursor solution changed from yellow to orange after being left overnight. The addition of SnF_2 (10, 20, 30, or 40 mol%) improved solution stability, as the mixed solutions retained their yellow color after overnight storage. XPS analysis was performed on pure $FASnI_3$ films and $FASnI_3$ films containing 20% SnF_2 prepared from solutions stored overnight, as shown in Fig. 2c. However, higher concentrations of SnF_2 led to significant phase segregation within the perovskite film, ultimately reducing device performance (Figs. 2d–2f). To address this issue, Lee et al. introduced pyrazine into the precursor solution (DMF/DMSO) and fabricated high-quality $FASnI_3$ films with excellent surface coverage and uniform morphology[26]. In this process, the nitrogen atoms in pyrazine coordinate with Sn^{2+}, which helps suppress phase separation and passivate Sn vacancies. This strategy produced dense, pinhole-free $FASnI_3$ layers and yielded a PCE of 4.8%[26]. Subsequently, Liao et al. reported efficient planar inverted $FASnI_3$ solar cells prepared through solvent engineering, achieving a PCE of 6.22%[27]. Building on these advances, Ke et al. incorporated ethylenediamine

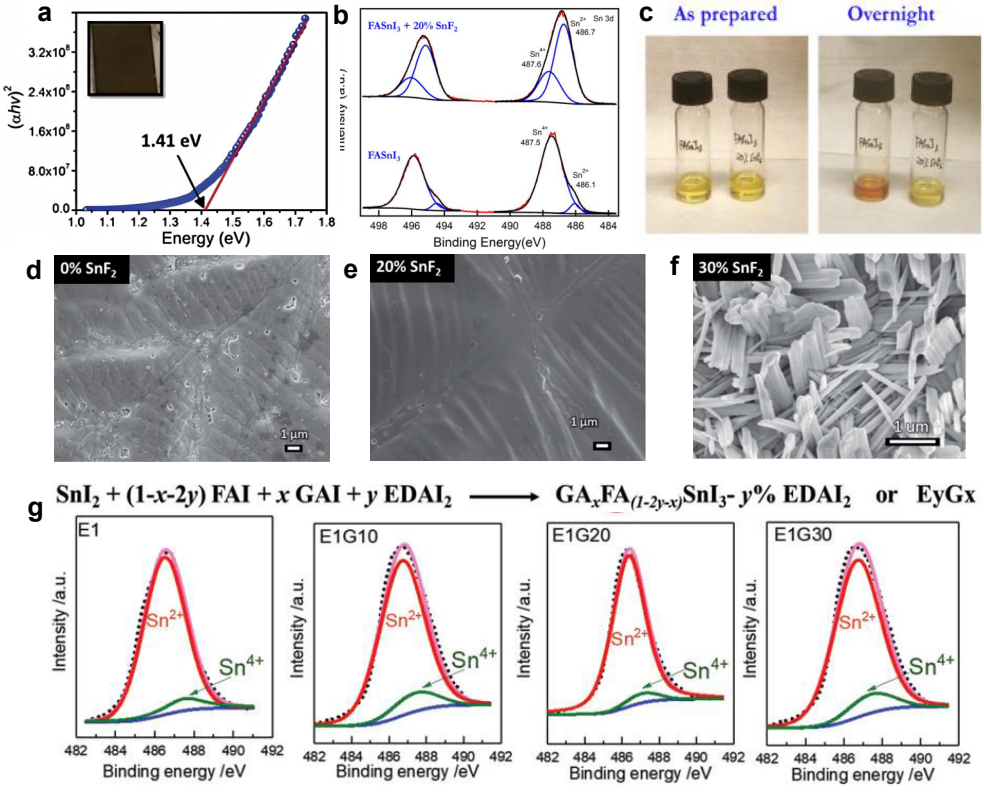

Figure 2 (a) Tauc plot of the $FASnI_3$ film showing the absorption onset, with the inset displaying an image of the $FASnI_3$ film. (b) XPS spectra of $FASnI_3$:20%SnF_2 and pure $FASnI_3$ films deposited from precursor solutions stored overnight under glovebox conditions, where the latter shows a pronounced Sn^{4+} signal. (c) Photographs showing the color change of the $FASnI_3$ precursor solution without SnF_2 addition. Top-view FESEM images of $FASnI_3$ (d) and $FASnI_3$:20%SnF_2 (e) perovskite films deposited on a mesoporous TiO_2 layer. (f) Enlarged view of the nanoplatelet-like structure observed on the surface of $FASnI_3$:30%SnF_2. Reproduced with permission from Ref. [22] ©2015, The Royal Society of Chemistry. (g) High-resolution X-ray photoelectron spectra (Sn 3d) of the surface of E1Gx films with x = 0, 10, 20, and 30 (EyGx denotes $GA_xFA_{1-x-2y}SnI_{3-y}EDAI_2$). Reproduced with permission from Ref. [33] ©2018, WILEY-VCH Verlag GmbH & Co. KGaA, Weinheim.

(en) cations into Sn-based perovskites, where en acts as an additional A-site component within the $FASnI_3$ framework, forming a mixed perovskite {en}$FASnI_3$[28]. This modification enabled bandgap tuning from 1.3 to 1.9 eV, and resulted in a PCE of 6.63% for the device containing 10% en compared with pristine $FASnI_3$.

In addition to the strategies discussed above, mixed-cation metal halide perovskites have been widely employed in Pb-based PSCs and have inspired similar approaches for Sn-based systems[29,30]. For example, Liu et al. demonstrated that MA and Cs can function as mixed A-site cations in Sn-based perovskites[31]. However, unoptimized $MA_{0.9}Cs_{0.1}SnI_3$ solar cells achieved a PCE of only 0.33%. Subsequently, Zhao et al. reported a 3D Sn-based perovskite incorporating mixed MA and FA cations[32], demonstrating that the FA-to-MA ratio significantly influences the material's optical properties and bandgap. The combined use of FA and MA improved film morphology and reduced charge-carrier recombination, resulting in a maximum PCE of 8.12% for $FA_{0.75}MA_{0.25}SnI_3$ with 10 mol% SnF_2. Beyond commonly used cations such as MA, FA, and Cs, researchers have also explored the incorporation of other organic cations. For example, Jokar et al. introduced varying amounts of the guanidinium cation (GA^+) into the $FASnI_3$ perovskite structure, together with 1% ethylenediammonium diiodide ($EDAI_2$) as an additive (Fig. 2g)[33]. The optimal performance was achieved at a precursor ratio of guanidinium iodide (GAI) to formamidinium iodide (FAI) of 20:80, yielding an initial PCE of 8.5%, which increased to 9.6% after 2000 h of storage in a glovebox. To date, the highest efficiencies in Sn-based PSCs have generally been reported for mixed-cation systems[34]. Wang et al. further improved device performance by introducing a novel additive, 5-mercapto-1-methyltetrazole tin salt (SnT_2). This additive modulated the bulk energy levels of the perovskite, with the valence and conduction bands shifting downward by 0.11 and 0.07 eV, respectively, thereby improving energy-level alignment with the charge-transport layers while simultaneously passivating iodine and tin vacancies. As a result, SnT_2 promoted grain growth (from an average of 284 to 417 nm) and reduced film roughness, leading to a PCE of 15.33%[34].

Although Sn-based organic–inorganic hybrid perovskites such as $CH_3NH_3SnI_3$ exhibit promising optoelectronic properties and offer a potential alternative to Pb-based perovskites, significant challenges remain. Poor stability and limited charge-carrier mobility continue to hinder their practical application. While strategies such as halide substitution and solvent engineering have led to some improvements, further optimization is required to overcome instability and limited device efficiency. Future

research is expected to focus on improving film quality, enhancing material stability, and optimizing interface engineering to increase device efficiency and reliability for large-scale commercialization.

2.2 Low-dimensional Sn halide perovskite

The development of Sn-based organic–inorganic hybrid perovskites has shown significant potential for addressing the toxicity concerns associated with Pb-based materials. However, these materials still face several limitations. An alternative strategy involves low-dimensional Sn halide perovskites, which may improve the stability and performance of Sn-based perovskite devices. Low-dimensional Sn halide perovskites generally refer to two-dimensional (2D) or quasi-2D structures that exhibit distinct structural and electronic characteristics compared with their 3D counterparts. Studies have shown that the incorporation of larger spacer cations can significantly enhance the stability of Sn-based perovskites[35,36]. In particular, bulky organic ammonium cations such as phenylethylammonium (PEA), butylammonium (BA), 2-hydroxyethylammonium (HEA), and guanidinium (GA) have been reported to suppress moisture ingress at the edges of layered Pb-based perovskites, thereby improving the stability of films and devices. These large organic cations typically act as spacer layers between perovskite slabs, resulting in the formation of layered perovskite structures[37]. This strategy can readily lead to the formation of low-dimensional (quasi-2D) and mixed-dimensional (2D/3D) perovskite structures, as illustrated in Fig. 3a. In general, 2D perovskites can be described by the formula $(A')_m(A)_{n-1}B_nX_{3n+1}$, where A' represents a bulky organic spacer cation. Depending on its valence, monovalent (m = 2) or divalent (m = 1) cations can be inserted between the anionic layers of the perovskite sheets[37]. Layered 2D halide Pb-based perovskites were first reported for PSC applications in 2014. For example, Smith et al. fabricated 2D layered perovskites using PEA and MA cations as the absorber layer, achieving a PCE of 4.73% with a high open-circuit voltage of 1.18 V and excellent moisture resistance in $(PEA)_2(MA)_2[Pb_3I_{10}]$ PSCs[35]. The promising performance of these 2D halide Pb-based perovskites has stimulated further investigation of analogous 2D Sn-based systems. For instance, Cao et al. demonstrated that 2D Sn-based perovskite $(BA)_2(MA)_{n-1}Sn_nI_{3n+1}$ solar cells exhibit improved performance and stability compared with their 3D counterparts[38].

Liao et al. reported the incorporation of mixed FA and PEA cations in low-dimensional Sn-based perovskites, where PEA functions as an organic spacer. As the PEAI content increases, the perovskite film evolves from a 3D structure to a mixed 2D/3D phase and eventually to a pure 2D structure (Fig. 3b). These low-dimensional Sn perovskites, protected by PEA spacer layers, exhibit significantly improved stability in ambient air compared with their 3D counterparts. Furthermore, the orientation of perovskite domains can be controlled by adjusting the PEA ratio. A highly vertically oriented perovskite film was

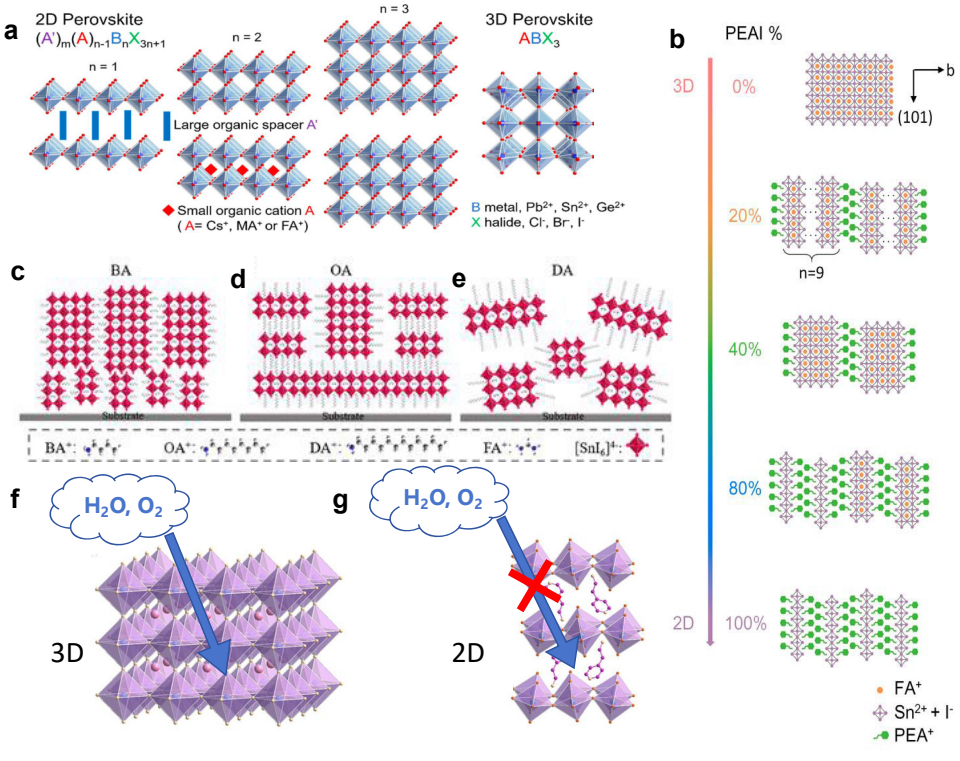

Figure 3 (a) Schematic illustration of the structural evolution from 2D to 3D perovskites.Reproduced with permission from Ref. [37] ©2019, American Chemical Society. (b) Crystal structures of $FASnI_3$, $(PEA)_2SnI_4$, and mixed FA–PEA Sn perovskites. Reproduced with permission from Ref. [39] ©2017, American Chemical Society. (c–e) Crystal orientation, dimensionality, and phase distribution of 2D perovskite films using different spacer cations: (c) BA, (d) OA, and (e) DA. Reproduced with permission from Ref. [40] ©2020, American Chemical Society. Schematic illustration of moisture and oxygen diffusion in 3D (f) and 2D (g) Sn-based perovskites. Adapted with permission from Ref. [36] ©2024, The Royal Society of Chemistry and the Chinese Chemical Society.

obtained with 20% PEA incorporation, which not only improved stability but also facilitated charge transport. Consequently, $FASnI_3$ PSCs containing 20% PEA achieved a maximum PCE of 5.94% with enhanced device stability[39]. Recently, Li et al. investigated the influence of alkyl chain length on the crystal growth of 2D Sn-based perovskites by introducing different alkylammonium spacer cations—butylammonium (BA), octylammonium (OA), and dodecylammonium (DA)—to fabricate 2D Sn perovskite films[40]. Their results indicate that shorter alkyl chains promote vertical crystal growth, which suppresses Sn^{2+} oxidation and improves charge transport. In contrast, longer alkyl chains favor horizontal crystal growth, which adversely affects device performance, as illustrated in Figs. 3c–3e. Consequently, PSCs based on BA achieved the highest PCE of 4.04% with minimal hysteresis[41].

Recently, Li et al. introduced PEACl to synthesize 2D Sn-based perovskites and investigated the effect of annealing temperature on crystal orientation within the perovskite films[42]. Their results showed that the proportion of the low-n 2D phase decreases with increasing annealing temperature (100 °C), while vertically oriented high-n 2D crystals become dominant. This vertical orientation is advantageous for charge transport. Similarly, Yu et al. significantly improved the performance of Sn-based PSCs by introducing a 2D/3D heterostructure, achieving an efficiency of 9.1%[43]. In this approach, 4-fluorophenylethylammonium bromide (FPEABr) partially replaced FAI in $FASnI_3$ to form a heterostructure in which 2D phases encapsulate the 3D grains and are located at surfaces and grain boundaries. This structure effectively suppressed Sn^{2+} oxidation, reducing the Sn^{4+} content from 15.8% to 7.8%, and decreased defect density, with trap density reduced from 6.20×10^{15} cm^{-3} to 3.32×10^{15} cm^{-3}. Consequently, the optimized 2D/3D film improved energy-level alignment and carrier extraction efficiency, increasing device performance from 9.38% to 14.81%. In 2025, Chen et al. introduced spatially isomeric fulleropyrrolidines (PPF2, PPF3, and PPF4) as additives in Sn-based PSCs to regulate the crystallization process[44]. By varying the spatial distance between the pyridine groups, these fulleropyrrolidines effectively control the colloid size in the perovskite precursor solution, thereby slowing the crystallization process and enabling the formation of high-quality films with reduced defect density and lower exciton binding energy. The device incorporating PPF4 achieved a certified efficiency of 16.05%, surpassing the 16% efficiency threshold for Sn-based PSCs for the first time. Recently, Li et al. developed a strategy to enhance the performance and stability of inverted Sn-based PSCs by introducing a molecular film at the buried interface to optimize the hole transport layer (HTL)[45]. Based on (E)-(2-(4',5'-bis(4-(bis(4-methoxyphenyl)amino)phenyl)-[2,2'-bithiophen]-5-yl)-1-cyanovinyl)phosphonic acid (MBP), this interfacial layer improves hole extraction and film quality. As a result, the device achieved a record PCE of 17.89% (certified 17.71%) for small-area devices and 14.40% for large-area (1 cm^2) devices, representing the highest reported efficiency in this field. The enhanced stability of 2D Sn-based perovskites can be attributed to both increased crystallographic rigidity and the physical barrier effect provided by hydrophobic organic spacer layers. These bulky organic layers form alternating inorganic–organic stacking structures that effectively inhibit the diffusion of oxygen and moisture toward the Sn^{2+}-containing octahedral framework (Figs. 3f and 3g). By restricting the penetration of external oxidants into the lattice, the oxidation of Sn^{2+} to Sn^{4+} can be significantly suppressed.

Low-dimensional Sn halide perovskites, including 2D and quasi-2D structures, provide a promising pathway for improving the stability of Sn-based perovskites. These materials exhibit enhanced resistance to moisture ingress and improved structural stability, making them attractive candidates for long-term applications. Consequently, they have become an increasingly common focus in the development of Sn-based perovskite materials. Looking ahead, optimizing the dimensional structure of perovskites may enable the simultaneous improvement of stability and efficiency while facilitating better charge-carrier transport. In addition, further investigations into the mechanisms associated with different organic spacer cations would provide valuable insights for the rational design of high-performance Sn-based perovskite solar cells.

2.3 Sn-based all-inorganic halide perovskite

Cesium tin halides, particularly $CsSnI_3$, have recently attracted significant attention due to the suitability of the Cs^+ ion for forming a stable 3D perovskite structure, as predicted by the tolerance factor (t). In this context, $CsSnX_3$ (where X = I, Br) are inorganic Sn-based perovskites that exhibit optical and electronic properties comparable to those of $FASnI_3$ and $MASnI_3$. Notably, the fully inorganic perovskite $CsSnI_3$ demonstrates improved thermal stability compared with mixed organic–inorganic Sn halide perovskites[46]. Scaife et al. first reported the characterization of halide Sn-based perovskites, including the fully inorganic $CsSnX_3$ compounds, in 1974[47]. Subsequently, Chen et al. demonstrated the use of $CsSnI_3$ as a solar cell absorber layer[48]. In their study, a simple layered Schottky solar cell structure consisting of indium tin oxide (ITO)/$CsSnI_3$/Au/Ti on a glass substrate was fabricated, achieving a PCE of 0.9% (Fig. 4a). Later, Kumar et al. reported $CsSnI_3$-based PSCs with a mesoporous device architecture[49]. However, pure $CsSnI_3$ may not be suitable as a solar cell absorber due to its high carrier concentration arising from intrinsic Sn vacancies. To improve device performance, the incorporation of SnF_2 into $CsSnI_3$ has been widely employed to suppress the formation of Sn vacancies and increase film resistance. In this regard, $CsSnI_3$ PSCs containing 20% SnF_2 exhibit a broad absorption range extending to approximately 950 nm, achieving a PCE of 2.02% and a J_{sc} of up to 22.7 mA cm^{-2} (Figs. 4b and 4c). In addition, the bandgap of $CsSnX_3$ can be tuned from 1.3 eV for $CsSnI_3$ to 1.7 eV for $CsSnBr_3$ (Fig. 4d)[50,51]. Correspondingly, the crystal structure transitions from an orthorhombic structure in $CsSnI_3$ to a cubic structure in $CsSnBr_3$ (Figs. 4d and 4e).

$CsSnI_3$, $CsSnBr_3$, and their mixed-halide variants are promising candidates for solar cell applications due to their favorable thermal and ambient stability. Notably, increasing the annealing temperature can significantly enlarge the grain size of $CsSnI_3$ films (Fig. 4f)[52]. This controlled grain growth, combined with optimized energy band alignment at device interfaces, facilitates more effi-

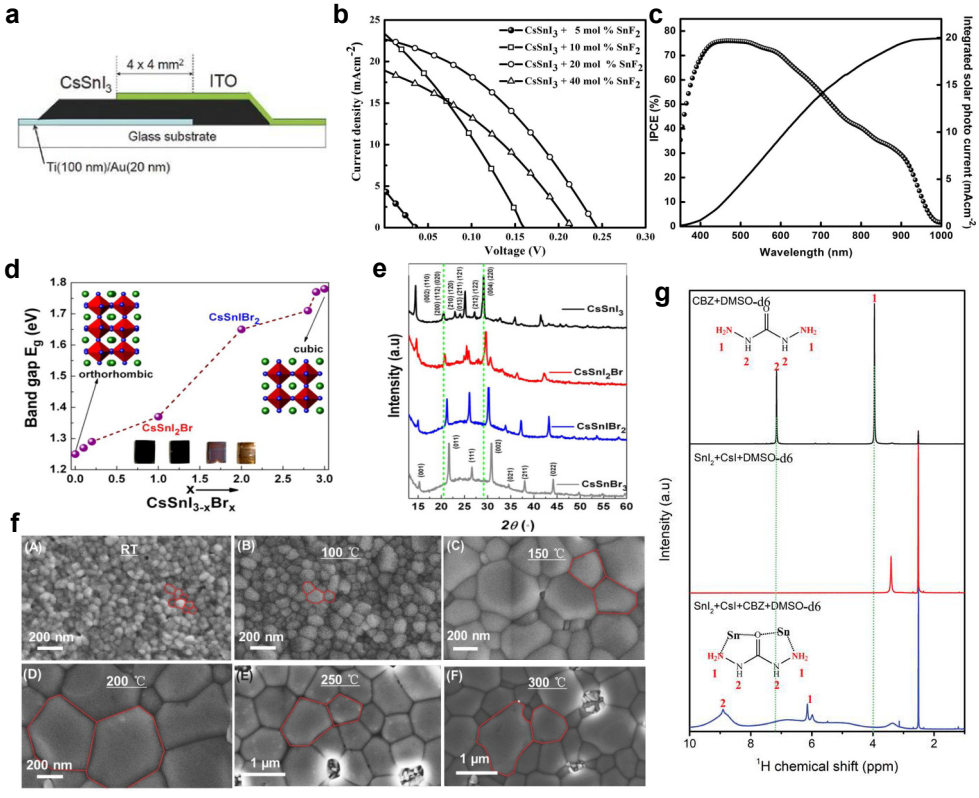

Figure 4 (a) Device structure of a Schottky solar cell based on $CsSnI_3$ perovskite. Reproduced with permission from Ref. [48] ©2012, American Institute of Physics. (b) *J*–*V* curves of photovoltaic devices demonstrating the effectiveness of SnF_2 incorporation. (c) Representative incident photon-to-current efficiency (IPCE) spectra of 20% SnF_2–$CsSnI_3$ devices, showing a photocurrent response extending into the infrared region (~950 nm). Reproduced with permission from Ref. [49] ©2014, WILEY-VCH Verlag GmbH & Co. KGaA, Weinheim. Bandgap variation (d) and XRD patterns (e) of $CsSnI_{3-x}Br_x$ (x = 1, 2, 3). Reproduced with permission from Ref. [51] ©2015, American Chemical Society. (f) SEM images of B-γ-$CsSnI_3$ films treated at different temperatures for 2 min. Reproduced with permission from Ref. [52] ©2016, WILEY-VCH Verlag GmbH & Co. KGaA, Weinheim. (g) ^{1}H NMR spectra of CBZ, $CsSnI_3$, and $CsSnI_3$:CBZ samples in DMSO-d6 solution. Reproduced with permission from Ref. [55] ©2023, Wiley-VCH GmbH.

cient electron and hole extraction. As a result, $CsSnI_3$-based PSCs have achieved a record-high PCE of 3.31% with a V_{oc} of 0.52 V, highlighting the importance of microstructure engineering and rational device design for high-performance lead-free $CsSnI_3$ solar cells. Recently, Marshall et al. reported the successful incorporation of $SnCl_2$ additives into $CsSnI_3$-based PSCs, achieving a best-performing device with a PCE of 3.56%[53]. In addition, Yin et al. proposed the use of thiourea derivatives as surface passivation agents to enhance the optoelectronic properties of $CsSnI_3$ perovskite films[54]. In this approach, Sn^{2+}-related defects present at both the surface and within the perovskite grains are effectively passivated, thereby reducing defect density and improving device performance. The resulting all-inorganic $CsSnI_3$ solar cells exhibited a PCE of 8.20% with improved stability, and the performance and stability of inorganic $CsSnI_3$ PSCs were further enhanced by introducing the bifunctional additive carbazole (CBZ)[54]. The $-NH_2$ and –CO functional groups of CBZ coordinate with Sn^{2+} to form five-membered ring structures (Fig. 4g), which delay crystallization and promote the formation of pinhole-free films, reducing the surface roughness from 43 to 16 nm. Moreover, a two-step annealing process (80 °C for pre-crystallization and 150 °C for reduction) effectively removes uncoordinated CBZ and reduces Sn^{4+} to Sn^{2+} at elevated temperatures, decreasing the Sn^{4+}/Sn^{2+} ratio from 0.85 to 0.20. After optimization, the device achieved a PCE of 11.21% (certified PCE of 10.90%) with a V_{oc} of 0.73 V and a J_{sc} of 21.38 mA cm^{-2}[55]. However, the intrinsic instability of Sn^{2+}, which readily oxidizes to Sn^{4+}, results in p-type self-doping in $CsSnI_3$ perovskites[55,56]. To address interfacial losses, Yu et al. introduced tetramethylcyclobutadiene-C_{60} (TMCB) as a novel electron-transport layer (ETL) for $CsSnI_3$-based PSCs[57]. By optimizing the energy-level alignment between the ETL and the perovskite layer, TMCB significantly reduces voltage losses and nonradiative recombination at the interface. Consequently, the $CsSnI_3$-based device incorporating TMCB achieved a record PCE of 14.95% with a high V_{oc} of 0.81 V, representing the highest reported efficiency for $CsSnI_3$ solar cells.

Compared with the previously discussed materials, all-inorganic Sn-based perovskites exhibit considerable application potential owing to their superior thermal stability and enhanced resistance to moisture. However, challenges such as limited charge-carrier mobility and the oxidation of Sn^{2+} remain critical issues that restrict their efficiency and long-term stability. Despite recent advances, including surface passivation and the incorporation of SnF_2 additives, the relatively lower performance of these materials compared with their Pb-based counterparts indicates that further strategies are required. These may include grain

size engineering and improved control over the crystallization process.

To address the complex oxidation processes in Sn-based perovskites, researchers have explored various strategies, including additive engineering, surface passivation, and the fabrication of low-dimensional perovskites. These approaches can effectively suppress Sn^{2+} oxidation and reduce trap defects, thereby improving the operational stability and performance of Sn-based PSCs. One widely adopted strategy is the incorporation of antioxidant additives. For example, the addition of SnF_2 to SnX_2 (where X = F, Cl) systems can effectively inhibit the oxidation of Sn^{2+} to Sn^{4+}, thereby reducing the background carrier density[49]. In addition to inorganic additives, hydrazine and other organic additives have also been reported to suppress Sn oxidation in SnX_2 and their derivatives. In particular, hydrazine and its derivative, hydrazinium dihydrochloride, can suppress the formation of Sn^{4+} impurities, thereby passivating defect states and reducing hysteresis in Sn-based PSCs[58]. Furthermore, while antioxidant additives primarily suppress the oxidation of Sn^{2+} in Sn-based PSCs, surface passivation strategies mitigate the detrimental effects of defects at grain boundaries and at the interfaces between the perovskite layer and charge-transport layers (CTLs)[54]. In this context, the development of low-dimensional perovskites has also proven effective in enhancing the stability and performance of Sn-based perovskites[41–43]. Recent advancements in interface engineering for high-efficiency Pb-based PSCs have demonstrated that strategies such as interface dipole modulation, energy-level alignment, and molecular passivation play critical roles in suppressing nonradiative recombination. Although these studies primarily focus on Pb-based systems, the underlying principles, including interfacial modification, the construction of electron-transport bridges, and the optimization of energy-level alignment, are also applicable to lead-free PSCs. Therefore, integrating these well-established interfacial engineering strategies into Sn-based and other lead-free systems may provide an effective pathway for further enhancing device performance[59,60]. For a comprehensive comparison, the photovoltaic performance parameters of representative Sn-based PSCs are summarized in Table 1 . Despite the increasing research efforts in this field, the efficiency of Sn-based PSCs remains significantly lower than that of their Pb-based counterparts, and these devices continue to suffer from poor ambient stability.

3 Sn–Pb-based PSCs

3.1 Sn–Pb-based single-junction cells

Although the development of completely lead-free perovskites remains the ultimate goal, low-lead Sn–Pb hybrid perovskites represent an important intermediate strategy for balancing environmental concerns with high device performance and stability. The moderate incorporation of Pb has proven effective in addressing several challenges associated with pure Sn-based perovskites. On the one hand, Pb incorporation compensates for the poor

Table 1 Performance summary of representative Sn-based PSCs

Type	Device structure	V_{oc} (V)	J_{sc} (mA cm^{-2})	FF (%)	PCE (%)	Ref.
Sn-based organic–inorganic hybrid perovskite	FTO/c-TiO_2/mp-TiO_2/$MASnI_3$/spiro-OMeTAD/Au	0.88	16.8	42	6.4	10
	FTO/c-TiO_2/mp-TiO_2/$MASnIBr_2$/spiro-OMeTAD/Au	0.82	12.3	57	5.73	11
	FTO/c-TiO_2/mp-TiO_2/$MASnI_3$/spiro-OMeTAD/Au	0.32	21.4	46	3.15	19
	FTO/c-TiO_2/$MASnBr_3$/P3HT/Au	0.41	2	41	0.35	21
	FTO/c-TiO_2/$MASnBr_3$/P3HT/Au	0.498	4.27	49.1	1.12	21
	FTO/c-TiO_2/mp-TiO_2/$FASnI_3$/spiro-OMeTAD/Au	0.238	24.45	36	2.1	22
	ITO/PEDOT:PSS/$FASnI_3$/C_{60}/BCP/Ag	0.465	22.07	60.67	6.22	27
	FTO/c-TiO_2/mp-TiO_2/{en}$MASnI_3$/PTAA/Au	0.429	24.28	63.72	6.63	28
	ITO/PEDOT:PSS/$(FA)_{0.75}(MA)_{0.25}SnI_3$/$C_{60}$/BCP/Ag	0.61	21.2	62.7	8.12	32
	ITO/PEDOT:PSS/$GA_{0.2}FA_{0.8}SnI_3$+1%$EDAI_2$/C_{60}/BCP/Ag	0.619	21.2	72.9	9.6	33
	FTO/PEDOT:PSS/$(Cs_{0.02}(FA_{0.9}DEA_{0.1})_{0.98})_{0.98}EDA_{0.01}SnI_3$/$C_{60}$/BCP/Ag	0.8426	24.72	73.6	15.33	34
Low-dimensional Sn halide perovskite	ITO/NiO_x/$(PEA)_2(FA)_{n-1}Sn_nI_{3n+1}$/PCBM/Al	0.59	14.44	69	5.94	39
	FTO/c-TiO_2/mp-TiO_2/$(BA)_2(FA)_{n-1}Sn_nI_{3n+1}$/PTAA/Au	0.42	23.98	40	4.04	40
	ITO/NiO_x/$(PEA)_2(FA)_{n-1}Sn_nI_{3n+1}$/$C_{60}$/BCP/Ag	0.59	22.03	69	9.1	42
	ITO/PEDOT:PSS/$(FPEA)_2(FA)_{n-1}Sn_nI_{3n+1}$/ICBA/BCP/Al	0.84	24.91	71	14.81	43
	ITO/PEDOT:PSS/$PEA_{0.15}FA_{0.85}SnI_3$/C_{60}BB/PCBM/BCP/Ag	0.86	26.17	71.35	16.05	44
	ITO/NiO_x/MBP/$PEA_{0.1}FA_{0.9}SnI_3$/ICBA/BCP/Ag	0.99	22.48	80.66	17.89	45
Sn-based all-inorganic halide perovskite	FTO/c-TiO_2/mp-TiO_2/$CsSnI_3$/spiro-OMeTAD/Au	0.24	22.7	37	2.02	49
	ITO/NiO_x/$CsSnI_3$/PCBM/Al	0.52	10.21	62.5	3.31	52
	ITO/$CsSnI_3$/PCBM/BCP/Al	0.5	9.89	68	3.65	53
	ITO/PEDOT:PSS/$CsSnI_3$/C_{60}/BCP/Cu	0.63	19.7	66.1	8.2	54
	ITO/NiO_x/$CsSnI_3$:CBZ /ZnO/PCBM/Ag	0.73	21.38	71.99	10.9	55
	ITO/PTAA/$CsSnI_2Br$ /ICBA/BCP/Ag	0.75	22.2	71.29	11.87	56
	ITO/PEDOT:PSS/$CsSnI_3$/TMCB/BCP/Ag	0.81	24.95	0.74	14.95	57

stability and low carrier mobility of pure Sn-based perovskites; on the other hand, optimizing the compositional ratio enables high photovoltaic performance while minimizing lead content. This approach therefore allows high device efficiency while reducing lead-related environmental concerns. In this context, Sn–Pb-based PSCs, particularly $CH_3NH_3Sn_xPb_{1-x}I_3$, have demonstrated extended light absorption compared with pure Pb-based systems. For example, $CH_3NH_3Sn_{0.5}Pb_{0.5}I_3$ exhibits a maximum absorption wavelength of up to 1060 nm as a result of significant bandgap tuning achieved by incorporating Sn into $CH_3NH_3PbI_3$ (Fig. 5a)[61]. Similarly, $CH_3NH_3Sn_xPb_{1-x}I_3$ perovskites display unusual bandgap behavior in which the bandgap decreases with increasing Sn content (Fig. 5b). A pronounced bandgap bowing effect has been observed in these mixed Sn–Pb perovskites, deviating from Vegard's law[62]. Consequently, the bandgap can be tuned within the range of approximately 1.2–1.6 eV (Fig. 5c), making these materials attractive light absorbers approaching the Shockley–Queisser efficiency limit for single-junction solar cells[63]. However, many early devices employed TiO_2 as the ETL, which requires high-temperature annealing during fabrication. This processing requirement imposes strict substrate limitations and restricts the development of low-temperature fabrication techniques.

To address these challenges, inverted (p–i–n) device architectures have been widely explored for PSCs incorporating Sn–Pb alloy perovskites. For example, Zuo et al. prepared mixed $MAPb_{1-x}Sn_xI_3(Cl)$ perovskites using MAI, $PbCl_2$, and $SnCl_2$ precursors, achieving a PCE exceeding 10% for the first time in Sn–Pb mixed PSCs (Fig. 5d)[64]. In this system, DMSO acts as a coordinating solvent that regulates the crystallization of mixed Sn–Pb perovskites[65]. The strong coordination interaction between DMSO and metal iodides slows the reaction between MAI and SnI_2/PbI_2, thereby promoting improved crystallinity. Furthermore, DMSO improves film quality and device performance by mitigating the uneven distribution of Sn within the alloyed perovskite films. As a result, a planar inverted device architecture based on these optimized films achieved a PCE of 15.2%[65]. Zong et al. introduced a Lewis adduct additive, SnF_2·3FACl, which enables a

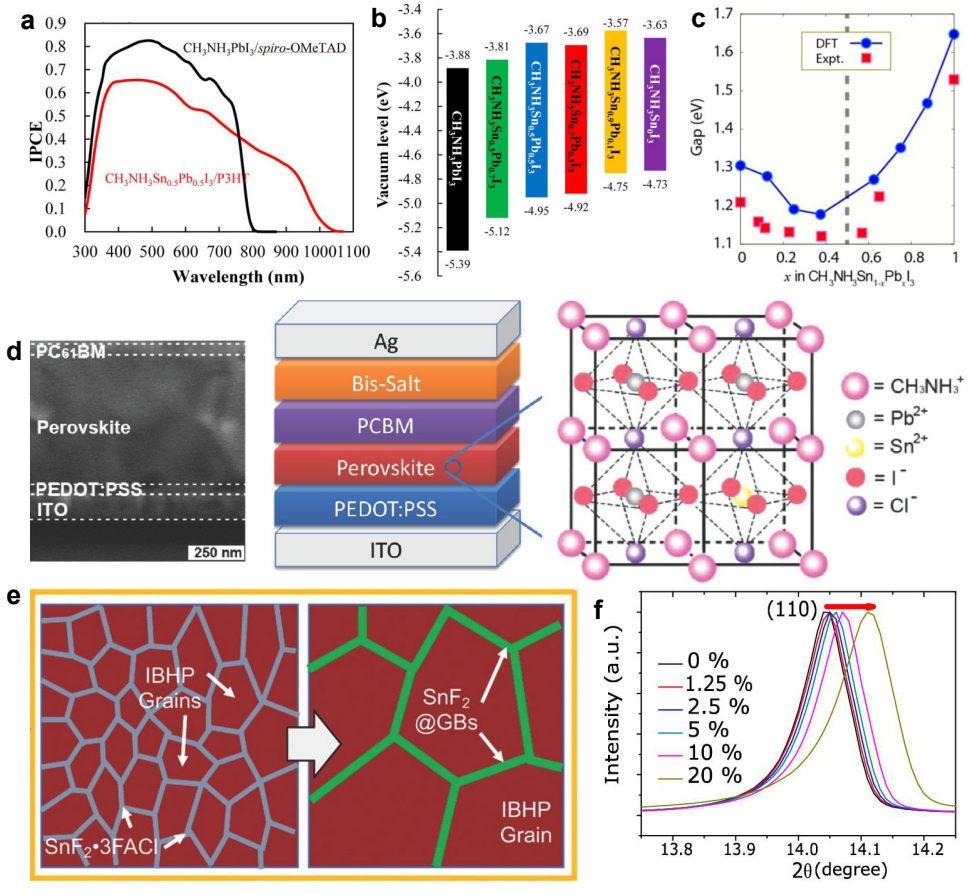

Figure 5 (a) IPCE spectra of PSCs based on $CH_3NH_3Sn_{0.5}Pb_{0.5}I_3$ and $CH_3NH_3PbI_3$. (b) Energy-level diagram of $CH_3NH_3Sn_xPb_{1-x}I_3$ perovskites. Reproduced with permission from Ref. [61] ©2014, American Chemical Society. (c) Experimental and calculated bandgap evolution of $CH_3NH_3Sn_{1-x}Pb_xI_3$ solid solutions as a function of composition x. Reproduced with permission from Ref. [62] ©2015, American Chemical Society. (d) Cross-sectional SEM image of a planar heterojunction solar cell and the crystal structure of $MAPb_{1-a}Sn_aX$. Reproduced with permission from Ref. [64] ©2014, WILEY-VCH Verlag GmbH & Co. KGaA, Weinheim. (e) Schematic illustration of grain-boundary functionalization in IBHP thin films mediated by Lewis adducts. Reproduced with permission from Ref. [66] ©2018, WILEY-VCH Verlag GmbH & Co. KGaA, Weinheim. (f) XRD patterns showing that the (110) peak shifts toward higher 2θ values with increasing Cs content in $(Cs_xFA_{1-x}SnI_3)_{0.5}(MAPbI_3)_{0.5}$. Reproduced with permission from Ref. [69] ©2019, American Chemical Society.

continuous distribution of SnF_2 along the grain boundaries of Sn–Pb perovskites, thereby improving their physical properties[66]. In this system, Lewis acid–base interactions between SnF_2 and FACl form a coordination complex that becomes unstable at elevated temperatures. The subsequent release of the FACl byproduct results in a uniform redistribution of SnF_2 along the grain boundaries of the alloyed perovskite films (Fig. 5e). Furthermore, the Sn-rich grain boundaries suppress the formation of Sn vacancies, thereby enhancing the chemical stability of the Sn–Pb mixed perovskite films. As a result, device performance improved from 12.9% to 15.8%, accompanied by enhanced environmental stability.

A recent study reported the fabrication of Sn–Pb binary PSCs via a galvanic displacement reaction (GDR)[67]. In this approach, Sn metal powder was introduced into a pure Pb-based perovskite precursor solution, generating an Sn–Pb binary precursor through the reaction: $Sn(s) + Pb^{2+} \rightarrow Sn^{2+} + Pb(s)$. XRD patterns and PL spectra confirmed the formation of $MAPb_{1-x}Sn_xI_3$ films, and the corresponding inverted device based on $MAPb_{0.4}Sn_{0.6}I_3$ achieved a PCE of 15.85%. Another study reported a PCE of 18.21% for devices based on $(FAPb_{0.6}Sn_{0.4}I_3)_{0.85}(MAPb_{0.6}Sn_{0.4}Br_3)_{0.15}$[67], highlighting the potential of the GDR strategy for fabricating mixed-metal PSCs. Similarly, Lin et al. synthesized narrow-bandgap Sn–Pb perovskites using the same GDR method[68]. In this system, metallic Sn powder suppresses the oxidation of Sn^{2+} through the reaction $Sn + Sn^{4+} \rightarrow 2Sn^{2+}$. As a result, device efficiency increased from 18.3% to 21.1%, representing one of the highest efficiencies reported for Sn–Pb mixed PSCs. In addition, Kapil et al. incorporated Cs into the lattice of $(FASnI_3)_{0.5}(MAPbI_3)_{0.5}$ to reduce lattice strain and enhance intrinsic stability. This effect was evidenced by lattice shrinkage resulting from Cs^+ incorporation (Fig. 5f)[69]. Similarly, thermally stimulated current measurements revealed that the incorporation of Cs^+ reduced the densities of both shallow and deep trap states. Furthermore, fluorine-doped tin oxide (FTO) glass was used instead of conventional ITO because FTO exhibits higher infrared transmittance, thereby enhancing the current density at wavelengths above 800 nm. Hu et al. recently developed a fully inorganic Sn–Pb mixed perovskite solar cell with a bandgap of 1.38 eV based on $CsPb_{0.6}Sn_{0.4}I_3$[70]. The stability of the $CsPb_{0.6}Sn_{0.4}I_3$ films was further improved by introducing SnF_2 as an antioxidant to passivate grain boundaries[66]. In addition, (4-aminomethyl)piperidinium diiodide ($(4AMP)I_2$) was employed to passivate surface defects and form a hydrophobic layer, resulting in a champion device PCE of 13.37%.

The limitations associated with film defects and efficiency bottlenecks were mitigated by introducing the non-covalent additive p-phenylenediamine (PPD), which regulates the asynchronous crystallization kinetics of Sn and Pb[71]. Density functional theory (DFT) and *ab initio* molecular dynamics calculations indicate that the stereochemically active lone-pair electrons of Sn^{2+} limit its coordination capability. PPD selectively interacts with Sn^{2+} through cation-π interactions, thereby suppressing rapid crystallization and promoting more uniform crystallization of Sn–Pb perovskite films. The resulting single-junction device achieved a certified efficiency of 24.13% (with a laboratory record of 24.5%), representing one of the highest efficiencies reported for Sn–Pb systems. Notably, the device retained 90% of its initial efficiency after 795 h of continuous light exposure under encapsulated conditions[71]. These studies collectively demonstrate that optimizing the Sn/Pb ratio through additive engineering in Sn–Pb-based single-junction PSCs can significantly enhance both efficiency and stability. The device structures and performance metrics of representative Sn–Pb single-junction PSCs are summarized in Table 2 . Such advances provide strong momentum toward the commercialization of lead-reduced PSCs and establish a solid foundation for the development of efficient Sn–Pb-based tandem solar cells.

3.2 Sn–Pb-based perovskite tandem cells

The design of Sn–Pb-based perovskite tandem solar cells is based on the principles of spectral matching and multi-junction synergy, aiming to surpass the efficiency limits of single-junction devices. In the solar spectrum, photon energies span a broad range, whereas single-junction cells absorb photons only within a limited energy window defined by their bandgap. As a result, photons with energies higher than the bandgap lose their excess energy as heat through thermalization, while photons with energies below the bandgap remain unabsorbed. Tandem solar cells address this limitation by stacking subcells with different bandgaps, enabling complementary absorption across the solar spectrum and thereby broadening the spectral response range[73]. Typically, a tandem device consists of a wide-bandgap top cell and a narrow-bandgap bottom

Table 2 Performance of Sn–Pb-based PSCs

Type	Device structure	V_{oc} (V)	J_{sc} (mA cm^{-2})	FF (%)	PCE (%)	Ref.
Sn–Pb-based single-junction cell	FTO/c-TiO_2/mp-TiO_2/$CH_3NH_3Sn_{0.5}Pb_{0.5}I_3$/P3HT/Au	0.42	20.04	50	4.18	61
	ITO/PEDOT:PSS/$MAPb_{0.85}Sn_{0.15}I_3$(Cl)/PCBM/Bis-C_{60}/Ag	0.77	19.5	67	10.1	63
	ITO/PEDOT:PSS/$MAPb_{0.75}Sn_{0.25}I_3$/C_{60}/ZrAcac/Ag	0.8	26.2	73	15.2	65
	ITO/PEDOT:PSS/$(FAPbI_3)_{0.7}(CsSnI_3)_{0.3}$/$C_{60}$/BCP/Ag	0.74	25.89	81	15.8	66
	ITO/PEDOT:PSS/$FA_{0.85}MA_{0.15}Pb_{0.6}Sn_{0.4}(I_{0.85}Br_{0.15})_3$/PCBM/Bis-$C_{60}$/Ag	0.87	26.45	79	18.21	67
	ITO/PEDOT:PSS/$MA_{0.3}FA_{0.7}Pb_{0.5}Sn_{0.5}I_3$/$C_{60}$/BCP/Cu	0.83	31.4	81	21.1	68
	FTO/PEDOT:PSS/$Cs_{0.025}FA_{0.475}MA_{0.5}Sn_{0.5}Pb_{0.5}I_3$/PCBM/$C_{60}$/BCP/Ag	0.81	33.14	76	20.4	69
	ITO/NiO_x/$CsPb_{0.6}Sn_{0.4}I_3$/4AMPI$_2$/PCBM/BCP/Ag	0.77	25.87	67	13.37	70
	FTO/PEDOT:PSS/$Rb_{0.04}Cs_{0.2}FA_{0.76}Pb_{0.5}Sn_{0.5}I_3$/$C_{60}$/BCP/Cu	0.895	33.55	81.59	24.5	71
	FTO/PEDOT:PSS/$Rb_{0.04}Cs_{0.2}FA_{0.76}Pb_{0.5}Sn_{0.5}I_3$/$C_{60}$/BCP/Cu	0.88	32.13	81.45	23.86	72

cell[74]. The wide-bandgap top cell absorbs high-energy photons, promoting electrons from the valence band to the conduction band. Meanwhile, lower-energy photons that pass through the top cell are subsequently absorbed by the narrow-bandgap bottom cell, generating additional charge carriers. Figure 6a illustrates this concept. By combining subcells with different bandgaps, tandem architectures improve photon utilization and enhance the overall PCE of the device. Consequently, a high-performance narrow-bandgap PSC is essential for all-perovskite tandem solar cells. Two main tandem architectures are commonly employed: two-terminal (2T) and four-terminal (4T) configurations (Figs. 6b and 6c). In the 2T architecture, the second subcell is monolithically fabricated on top of the first. In contrast, the 4T architecture consists of two independently fabricated subcells on separate substrates that are subsequently stacked and operated independently. In a 2T tandem device, the subcells are connected through a tunnel junction or recombination layer and share two external electrical contacts. At least one of these contacts must be semi-transparent to allow light to enter the device. By contrast, the 4T configuration connects each subcell independently to the external circuit, requiring four contacts per tandem device, three of which must be semi-transparent to enable light transmission to both subcells. Because semi-transparent contacts can absorb a portion of incident photons, the smaller number of such contacts in the 2T configuration provides a slight advantage in overall efficiency. However, 2T devices are more challenging to fabricate. This challenge is particularly significant for solution-processed tandem cells, where the solvent used to deposit the upper subcell may damage the underlying layers. Notably, most commercially deployed tandem solar cells adopt a monolithically interconnected 2T architecture[73].

Eperon et al. introduced Cs to improve the performance of mixed Sn–Pb PSCs[75]. An efficiency of 14.8% was achieved for $FA_{0.75}Cs_{0.25}Sn_{0.5}Pb_{0.5}I_3$, attributed to improved light absorption and film properties resulting from the incorporation of 25% Cs. When integrated with a wide-bandgap top cell, the tandem device reached a PCE of 17.0%, highlighting the critical role of the interconnection layer (ICL) in determining tandem device performance. The ICL not only protects the bottom cell during the fabrication of the top cell but also enables efficient charge recombination and extraction between the two subcells. Similarly, Palmstrom et al. introduced a thin layer of polyethyleneimine ethoxylated (PEIE) as a nucleation layer to improve the coverage of atomic layer deposition (ALD)-grown aluminum-doped zinc oxide (AZO)[76]. In this architecture, a dimethylammonium (DMA)-FA-cesium A-site alloyed perovskite ($FA_{0.6}Cs_{0.3}DMA_{0.1}PbI_{2.4}Br_{0.6}$), with a bandgap of 1.7 eV, served as the wide-bandgap top cell material. A two-terminal monolithic tandem device combining the narrow-bandgap $FA_{0.75}Cs_{0.25}Sn_{0.5}Pb_{0.5}I_3$ perovskite bottom cell with a C_{60}/PEIE/AZO/sputtered indium zinc oxide/PEDOT:PSS interconnection layer achieved a PCE of 23.1% on a rigid substrate (Fig. 6d). Moreover, fabrication on a flexible polyethylene naphthalate substrate yielded a high efficiency of 21.3%, demonstrating excellent mechanical flexibility and bending stability[76]. Lin et al. subsequently constructed a monolithic all-perovskite tandem device (Fig. 6e) following the successful development of a narrow-bandgap Sn–Pb PSC with a PCE of 21.1% using the GDR method[68].

Excellent current matching was achieved, with inte-

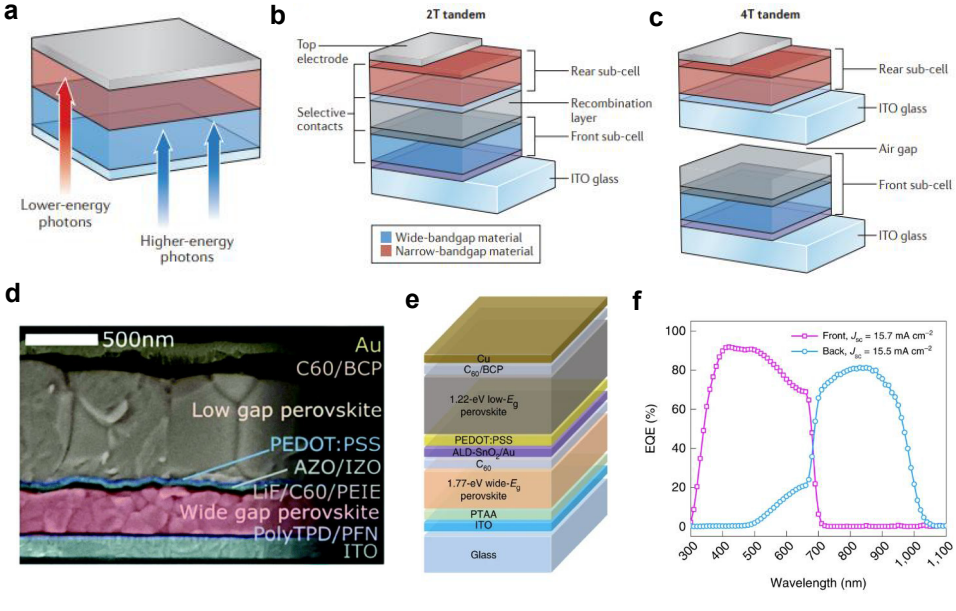

Figure 6 (a) Schematic illustration of tandem solar cells, where higher-energy photons are absorbed by the wider-bandgap semiconductor (blue) and lower-energy photons are absorbed by the narrower-bandgap semiconductor (red). Architectures of two-terminal (2T, b) and four-terminal (4T, c) tandem solar cells. Reproduced with permission from Ref. [73] ©2017, Macmillan Publishers Limited. (d) Cross-sectional SEM images of all-perovskite laminated solar cells. Reproduced with permission from Ref. [76] ©2019, Elsevier Inc. (e) Device structure of a series-connected solar cell. (f) External quantum efficiency spectrum of the best-performing small-area series cell, showing integrated J_{sc} values of 15.7 and 15.5 mA cm^{-2} for the front and rear subcells, respectively. Reproduced with permission from Ref. [68] ©2019, The Author(s), under exclusive licence to Springer Nature Limited.

grated current densities of approximately 15.7 and 15.5 mA cm^{-2} for the wide- and narrow-bandgap subcells, respectively. This resulted in a certified PCE of approximately 24.8% for the small-area device (0.049 cm^2) and 22.1% for the large-area device (1.05 cm^2), as shown in Fig. 6f[68]. Recently, 2-aminoethanesulfonic acid (taurine) was proposed as an interfacial bridge to enhance HTL-free low-bandgap PSCs[77]. This modification improved the optoelectronic properties of the perovskite absorber near the buried contact. Compared with conventional PEDOT:PSS HTLs, taurine-modified ITO substrates exhibited lower optical losses, improved energy-level alignment, and enhanced charge-transfer capability, resulting in increased open-circuit voltage and short-circuit current density. Another study reported a surface reconstruction strategy employing 1,4-butanediamine as a surface-polishing agent and ethylenediammonium diiodide ($EDAI_2$) to suppress Sn-related defects and passivate surface organic-cation and halide vacancies, thereby minimizing nonradiative recombination losses[78]. This strategy enabled the formation of high-quality Sn–Pb mixed perovskite films with surfaces approaching ideal stoichiometry, achieving PCEs of 22.65% and 23.32% for Sn–Pb PSCs with bandgaps of 1.32 and 1.25 eV, respectively. In summary, various strategies, including additive engineering and compositional tuning, have been developed to enable high-performance mixed Sn–Pb PSCs. Yuan et al. introduced tris(2-carboxyethyl)phosphine (TCEP) as a multifunctional redox shuttle in Sn–Pb mixed perovskite precursors[72]. This additive provides a suitable redox potential to accelerate the self-healing reaction between oxidized tetravalent tin (Sn^{4+}) and photogenerated zero-valent lead (Pb^0), thereby suppressing defect formation. In addition, TCEP coordinates with divalent tin (Sn^{2+}), regulating the crystallization kinetics of the perovskite and promoting the formation of high-quality films with reduced trap-state density. The resulting single-junction Sn–Pb mixed PSC achieved an optimal PCE of 23.86%. When integrated into a monolithic all-perovskite tandem device, the TCEP-treated narrow-bandgap subcell enabled a record tandem PCE of 28.86%. Currently, numerous devices have achieved efficiencies exceeding 20% while replacing more than 50% of lead with tin, indicating significant potential for reducing the toxicity of PSCs while maintaining high performance.

Although Sn–Pb-based PSCs show significant potential to balance environmental considerations with high performance, their practical application still faces several challenges. First, Sn^{2+} readily oxidizes to Sn^{4+} in air, leading to material degradation and performance loss. This is a common issue in Sn-based perovskites and a key factor limiting their long-term stability. Second, differences in the crystallization kinetics of Sn and Pb can lead to film inhomogeneity and increased defect density, which adversely affect carrier transport and device efficiency. Finally, most high-efficiency devices currently rely on complex additive engineering and precise interface control, which require further simplification and optimization for large-scale manufacturing.

Looking ahead, Sn–Pb-based perovskites represent a promising "low-lead" technological pathway. Advances in efficient antioxidant strategies, optimization of crystallization processes, and the development of stable low-dimensional/3D composite structures are expected to significantly enhance environmental stability while further improving device efficiency. In addition, the tunable bandgap of these materials makes them ideal candidates for narrow-bandgap bottom cells in all-perovskite tandem solar cells, which could potentially surpass the efficiency limit of single-junction devices predicted by the Shockley–Queisser limit. By systematically addressing key challenges at both the material and device levels, Sn–Pb hybrid perovskites are expected to play a central role in next-generation thin-film photovoltaic technologies that combine high efficiency, reduced toxicity, and commercial viability.

4 Other metal-based PSCs

4.1 $AB^{2+}X_3$ perovskites

In addition to the widely studied Sn- and Pb-based systems, other lead-free perovskite alternatives have attracted increasing interest. These materials involve replacing B-site Sn^{2+} and Pb^{2+} with other metal cations through divalent, trivalent, or tetravalent substitutions. For example, the tolerance factors (t) of $MAGeX_3$ materials that fully replace Pb are approximately 1.005 for $MAGeCl_3$, 0.988 for $MAGeBr_3$, and 0.965 for $MAGeI_3$, all of which fall within the ideal structural range for perovskite formation[79]. However, these materials face challenges similar to those of Sn-based perovskites, including susceptibility to oxidation and difficulties in controlling film morphology. Bandgap tuning can also be achieved by varying the A-site cations. For instance, $CsGeI_3$, $MAGeI_3$, and $FAGeI_3$ exhibit bandgaps of 1.63, 2.0, and 2.35 eV, respectively (Figs. 7a and 7b)[80]. To date, many studies on Ge-based PSCs have relied on device simulations using tools such as SCAPS and theoretical investigations based on DFT calculations[81–83], whereas relatively limited work has focused on experimental devices. For example, the $CsGeI_3$ solar cell reported by Krishnamoorthy et al. exhibited a low PCE of 0.2%, which was attributed to poor film quality and unoptimized charge-transport layers, as shown in Fig. 7c[80]. This remains far below the theoretical maximum efficiency of 27.9%. Introducing Br^- into methylammonium germanium iodide perovskites improved device performance, yielding a peak PCE of 0.57% for $MAGeI_{2.7}Br_{0.3}$-based devices. However, efficiency dropped to 0.21% within a few hours after fabrication[84], highlighting severe stability issues in Ge-based PSCs. The self-doping mechanisms in Sn- and Ge-based perovskites differ in both origin and impact. In Sn-based systems, Sn^{2+} oxidation to Sn^{4+} generates Sn vacancies, inducing strong p-type self-doping that increases background hole density and enhances nonradiative recombination. In contrast, Ge^{2+} is inherently more unstable, leading to rapid oxidation and the formation of deep defects. As a result, self-doping in Ge-based perovskites is more pronounced and associated with deeper trap states, further limiting carrier lifetime and device efficiency. Beyond oxidation and poor film quality, the broader application of Ge-based perovskites is constrained by the high cost and low natural abundance of

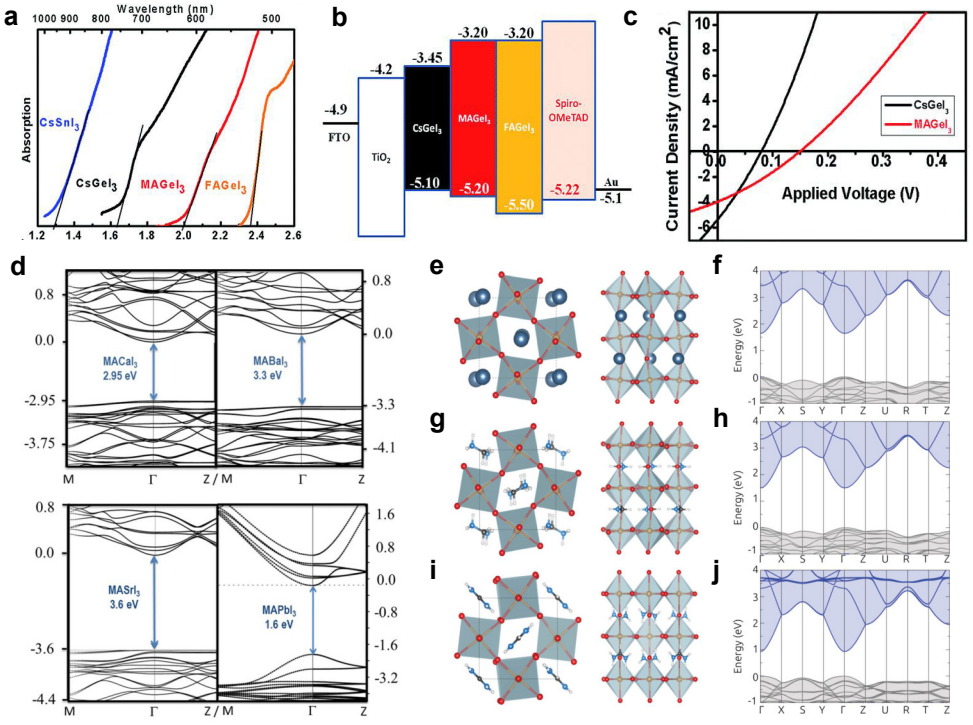

Figure 7 (a) Optical absorption spectra of $CsGeI_3$, $MAGeI_3$, and $FAGeI_3$ compared with $CsSnI_3$. (b) Schematic of the corresponding energy levels. (c) *J*–*V* curves of devices fabricated with different germanium halide perovskites. Reproduced with permission from Ref. [80] ©2015, The Royal Society of Chemistry. (d) Calculated band structures along the M–Γ–Z path for $MACaI_3$, $MABaI_3$, $MASrI_3$, and $MAPbI_3$. Energy scale labels apply only to CB and VB, not to the bandgap except for $MAPbI_3$. Reproduced with permission from Ref. [86] ©2016, American Physical Society. (e–j) Ball-and-stick models and band structures of hypothetical perovskites: $CsMgI_3$ (e, f), $CH_3NH_3MgI_3$ (g, h), and $CH(NH_2)_2MgI_3$ (i, j). Reproduced with permission from Ref. [87] ©2016, American Chemical Society.

germanium relative to lead and tin, posing an additional barrier to commercialization.

Despite significant progress, improving device stability remains a key focus for future research. Alkaline earth metals (Mg, Ca, Sr, Ba), along with certain transition metals such as Cu, have been considered as potential replacements for Pb, offering the possibility of maintaining stable perovskite structures compared with Group 14 elements like Sn and Ge. These divalent metals are abundant and represent promising Pb alternatives[85,86]. For example, the ionic radii of Mg^{2+}, Ca^{2+}, Sr^{2+}, and Ba^{2+} are approximately 0.072, 0.100, 0.118, and 0.135 nm, respectively. As the B-site ionic radius increases, the work function decreases, reducing electronegativity and widening the bandgap. Reported bandgaps of $MACaI_3$, $MASrI_3$, and $MABaI_3$ are 2.95, 3.6, and 3.3 eV, respectively (Fig. 7d). These materials exhibit large bandgaps and high hygroscopicity, limiting their suitability as light absorbers. By contrast, $FAMgI_3$, $MAMgI_3$, and $CsMgI_3$ have more favorable bandgaps of approximately 0.9, 1.5, and 1.7 eV, respectively, making them better candidates for photovoltaic applications (molecular models and bandgap structures are shown in Figs. 7e and 7j)[86,87].

4.2 $A_3B^{3+}{}_2X_9$ perovskites

While Sn and Ge are the primary candidates to replace Pb in PSCs, other B-site alternatives, including trivalent (B^{3+}) and tetravalent (B^{4+}) cations, also show promise. Trivalent cations such as Bi^{3+} and Sb^{3+} possess lone-pair electrons that influence the stoichiometry of the $A_3B_2X_9$ structure, often creating cation vacancies[88,89]. Compared to conventional ABX_3 perovskites, $A_3B_2X_9$ materials exhibit more complex crystal structures with diverse atomic arrangements in their unit cells. These compounds typically adopt dimerized or layered configurations characterized by isolated $[Bi_2I_9]^{3-}$ bioctahedra, whereas the layered variants resemble vacancy-ordered perovskites. For example, in $Cs_3Bi_2I_9$, $[BiI_6]^{3-}$ octahedra share faces to form $[Bi_2I_9]^{3-}$ units, resulting in a zero-dimensional (0D) molecular salt structure[88]. By contrast, $Cs_3Sb_2I_9$, $Rb_3Sb_2I_9$, and $Rb_3Bi_2I_9$ adopt 2D layered structures with corner-sharing $[BiI_6]^{3-}$ octahedra (Figs. 8a–8c). Notably, the crystals in $Cs_3Bi_2I_9$ and $MA_3Bi_2I_9$ lack corner-sharing octahedra while maintaining a stable perovskite stoichiometry[90]. The $6s^2$ lone pair of Bi^{3+}, isoelectronic with Pb^{2+}, further motivates interest in the crystal chemistry of bismuth-based halides[91]. For example, Park et al. investigated three bismuth halides—$Cs_3Bi_2I_9$, $MA_3Bi_2I_9$, and $MA_3Bi_2I_{9-x}Cl_x$—as light-absorbing materials in solar cells[92]. The optical bandgaps of these compounds are 2.2, 2.1, and 2.4 eV, respectively (Figs. 8d). Their absorption coefficients (~1×10^5 cm^{-1} at 450 nm) are comparable to $MAPbI_3$ (~2×10^5 cm^{-1} at 450 nm). $MA_3Bi_2I_{9-x}Cl_x$ particles are surrounded by a more gel-like matrix (Fig. 8e), while $MA_3Bi_2I_9$ forms interconnected thin layers approximately 50 nm thick (Fig. 8f). SEM images of $Cs_3Bi_2I_9$ (Fig. 8g) show hexagonal flakes, suggesting preferential crystal growth along the c axis. Compared to $MA_3Bi_2I_9Cl_x$, the $MA_3Bi_2I_9$ perovskite exhibits lower exciton and bandgap energies, likely due to the markedly different morphologies observed in SEM

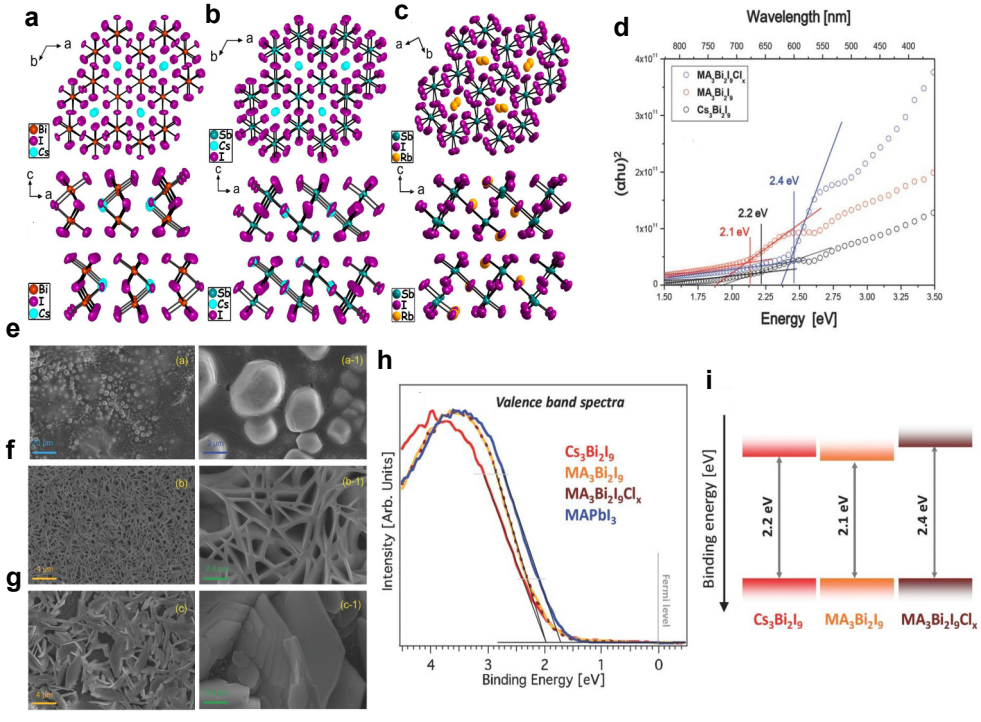

Figure 8 (a–c) Crystal structures of $Cs_3Bi_2I_9$, $Cs_3Sb_2I_9$, and $Rb_3Sb_2I_9$ observed along the *c* and *b* axes.Reproduced with permission from Ref. [88] ©2017, American Chemical Society. (d) Tauc plots of $MA_3Bi_2I_9Cl_x$, $MA_3Bi_2I_9$, and $Cs_3Bi_2I_9$ thin films. (e–g) SEM top-view images of the surface morphologies of the three bismuth-based materials: $MA_3Bi_2I_9Cl_x$ (e), $MA_3Bi_2I_9$ (f), and $Cs_3Bi_2I_9$ (g). (h) Valence band spectra measured by XPS using AlKα for $Cs_3Bi_2I_9$, $MA_3Bi_2I_9$, and $MA_3Bi_2I_9Cl_x$ (red, orange, and brown dotted lines, respectively), compared with $MAPbI_3$ (blue). Intensities at the valence band peaks are normalized for comparison. (i) Schematic illustrating the energy-level alignment between the Fermi level and valence/conduction bands, combining valence band positions from XPS and optical bandgaps from Tauc plots. Reproduced with permission from Ref. [92] ©2015, WILEY-VCH Verlag GmbH & Co. KGaA, Weinheim.

images. The interconnected layer structure of $MA_3Bi_2I_9$ may facilitate the formation of lower-energy excitons, in contrast to the more particle-like morphology of $MA_3Bi_2I_9Cl_x$. All three materials were analyzed using AlKα XPS. Figure 8h shows the valence band spectra of $MA_3Bi_2I_9$, $MA_3Bi_2I_9Cl_x$, and $Cs_3Bi_2I_9$ compared with the commonly used $MAPbI_3$ perovskite. The valence band edges of the bismuth-based materials exhibit similar binding energies relative to the Fermi level, with $MA_3Bi_2I_9$ and $MA_3Bi_2I_9Cl_x$ spectra nearly overlapping. By contrast, the linear fit of the $MAPbI_3$ valence band intersects at a lower binding energy. Combining the optical bandgaps with the valence band positions obtained from XPS allows construction of the schematic band diagram shown in Fig. 8i. A solar cell using $Cs_3Bi_2I_9$ as the light absorber achieved a PCE of approximately 1.09% and an open-circuit voltage of 0.85 V. Although this represented the highest reported efficiency for these materials at the time, it remains considerably lower than that of Pb-based perovskite devices.

$MA_3Bi_2I_9$ has attracted increasing attention due to its closer similarity to lead perovskites compared to Cs-based bismuth halides. Lyu et al. reported its use as a light absorber in solar cells, achieving a PCE of approximately 0.19% as a Pb-free alternative[93]. Subsequent optimizations in device architecture improved the efficiency of $MA_3Bi_2I_9$-based cells to 0.42%[94]. Buonassisi et al. synthesized phase-pure $MA_3Bi_2I_9$ via solution processing combined with a vapor-assisted technique to refine film morphology, as shown in Fig. 9a[95]. The resulting films demonstrated superior environmental stability relative to $MAPbI_3$, maintaining their appearance after 13 days in ambient air at room temperature (Fig. 9b). Furthermore, Hu et al. reported the first bulk heterojunction (BHJ) bismuth-based perovskite solar cell, featuring an active layer composed of in situ phase-separated $Cs_3Bi_2I_9$ and $Ag_3Bi_2I_9$ components (Fig. 9c), achieving a record PCE of ~3.6% and a notable open-circuit voltage of 0.89 V[96]. The $Cs_3Bi_2I_9$–$Ag_3Bi_2I_9$ BHJ device also exhibited excellent thermal stability, maintaining ~90% of its initial PCE after 450 h at 85 °C in a glovebox. Recently, a new class of lead-free perovskites incorporating potassium iodide (KI) into the precursor solution was investigated[97]. KI incorporation reduced the bandgap, enhanced material stability, and significantly improved photovoltaic performance. A PSC based on 2 vol.% KI-doped $Cs_3Bi_2I_9$ achieved the highest PCE among Bi-based devices (2.81%) with a V_{oc} of 1.01 V (Fig. 9d). Furthermore, these devices demonstrated remarkable moisture stability, retaining 98% of their initial PCE after 90 days (Fig. 9e).

Analogous to bismuth-based perovskites, antimony can form various structures by combining different organic or inorganic cations with halides. Saparov et al. investigated the lead-free layered perovskite $Cs_3Sb_2I_9$, which exhibited grain sizes exceeding 1 μm and an optical bandgap of 2.05 eV[98]. However, $Cs_3Sb_2I_9$ devices achieved a PCE below 1%, highlighting the need for further optimization due to its relatively wide bandgap, lower exciton binding

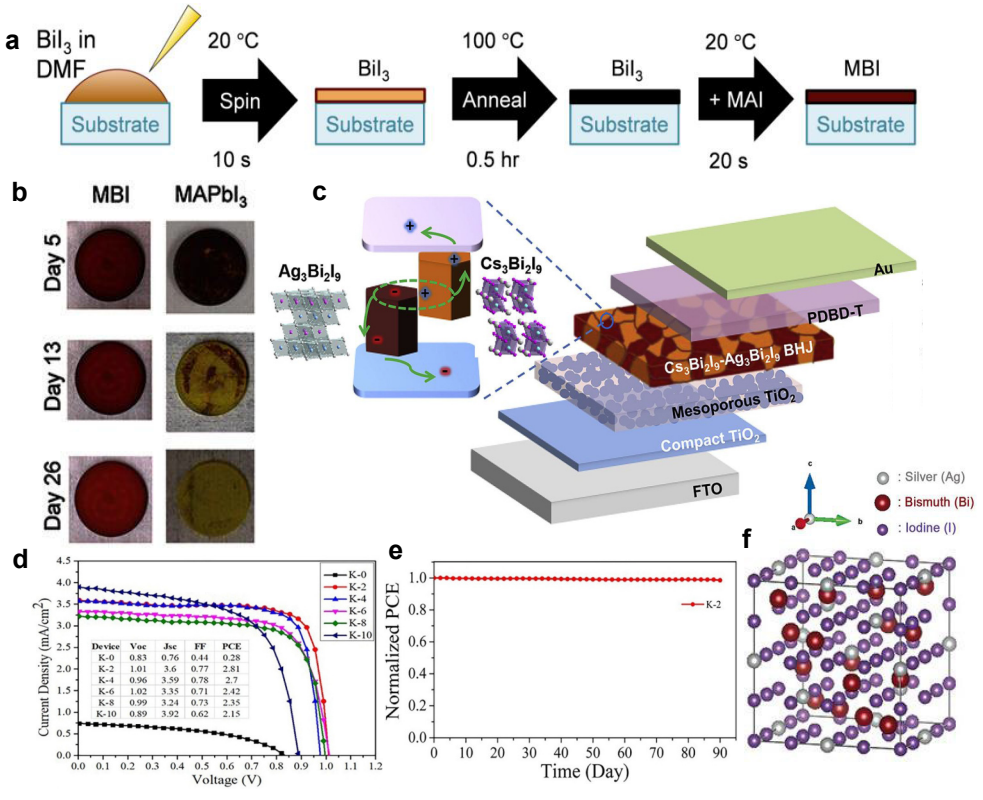

Figure 9 (a) Schematic of the solution-assisted fabrication process for $MA_3Bi_2I_9$ films. (b) Photographs showing the appearance of $MA_3Bi_2I_9$ and $MAPbI_3$ films in ambient air over time. Reproduced with permission from Ref. [95] ©2016, WILEY-VCH Verlag GmbH & Co. KGaA, Weinheim. (c) Device structure of the FTO/c-TiO_2/mp-TiO_2/BHJ bismuth-based perovskite/PDBD-T/Au solar cell. Reproduced with permission from Ref. [96] ©2019 Elsevier Ltd. (d) *J*–*V* curves and corresponding device parameters for K-0, K-2, K-4, K-6, K-8, and K-10 devices. (e) Normalized PCE of the K-2 device as a function of storage time in ambient air (0–90 days). Reproduced under the CC BY 4.0 license from Ref. [17] ©2022, The Authors. (f) Cubic crystal structure of $AgBi_2I_7$, showing the positions of silver, bismuth, and iodide atoms. Reproduced with permission from Ref. [99] ©2016, WILEY-VCH Verlag GmbH & Co. KGaA, Weinheim.

energy, and limited exciton diffusion length. To address these limitations, Kim et al. developed a solution-processing route for a pure cubic-phase iodobismuthate absorber, $AgBi_2I_7$, by spin-coating silver and bismuth precursors dissolved in *n*-butylamine, followed by annealing under nitrogen (Fig. 9f)[99]. This approach incorporates monovalent Ag^+ ions in place of alkali metal cations within the iodobismuthate framework, yielding a novel absorber material. Increasing the annealing temperature from 90 °C to 150 °C produced denser and more uniform crystalline films. Films annealed at 150 °C exhibited strong light absorption across 350–750 nm, achieving a PCE of 1.22%. Additionally, the use of antisolvents has proven effective for controlling nucleation and enhancing film quality. For example, green benzyl ether was employed as an antisolvent, yielding films with high crystallinity, dense surface morphology, and superior light absorption. The resulting champion device, fabricated with a low-cost carbon electrode, achieved a PCE of 2.07%[100], representing one of the highest reported efficiencies for inorganic Sb-based PSCs.

4.3 $A_2B^{4+}X_6$ perovskites

Beyond trivalent cations, perovskites incorporating tetravalent cations have been explored. These materials generally follow the formula $A_2B^{4+}X_6$, with representative B-site cations including Te^{4+}, Ti^{4+}, and Sn^{4+}[101]. Many of these structures are classified as double perovskites, where B^{4+} is paired with a vacancy. Most research has focused on their intrinsic optoelectronic properties, with relatively few studies investigating device applications. Inorganic tellurium-based perovskites, A_2TeI_6 (A = K, Rb, Cs, Tl), have attracted attention due to their low bandgaps of 1.38–1.52 eV[102]. For instance, Cs_2TeI_6 adopts a vacancy-ordered cubic double perovskite structure ($A_2B'B''X_6$), with Te^{4+} occupying the B' site and a vacancy at the B'' site. Similarly, Cs_2PdBr_6 exhibits a vacancy-ordered double perovskite structure, featuring a bandgap of 1.6 eV, black single-crystal morphology, and excellent structural and moisture stability, as shown in Figs. 10a and 10b[103].

Although Sn^{2+}-based perovskites are intrinsically unstable in air, Sn^{4+}-based perovskites have attracted renewed interest as solution-processable, air-stable, and non-toxic alternatives. A prominent example is Cs_2SnI_6, which combines a narrow direct bandgap with a high absorption coefficient while overcoming the stability limitations of Sn^{2+}-based counterparts[104,105]. Unlike the air-sensitive $CsSnI_3$, Cs_2SnI_6 contains Sn in the +4 oxidation state, providing enhanced stability under both ambient and moist conditions. Figure 10c illustrates a two-step solid-state deposition method for converting $CsSnI_3$ into Cs_2SnI_6 thin films. Notably, Cs_2SnI_6 adopts the same crystal structure as Cs_2PdBr_6 (Fig. 10b). The bandgap of Cs_2SnI_6 thin films ranges from 1.3 to 1.6 eV depending on the processing method and can be further tuned from 1.3

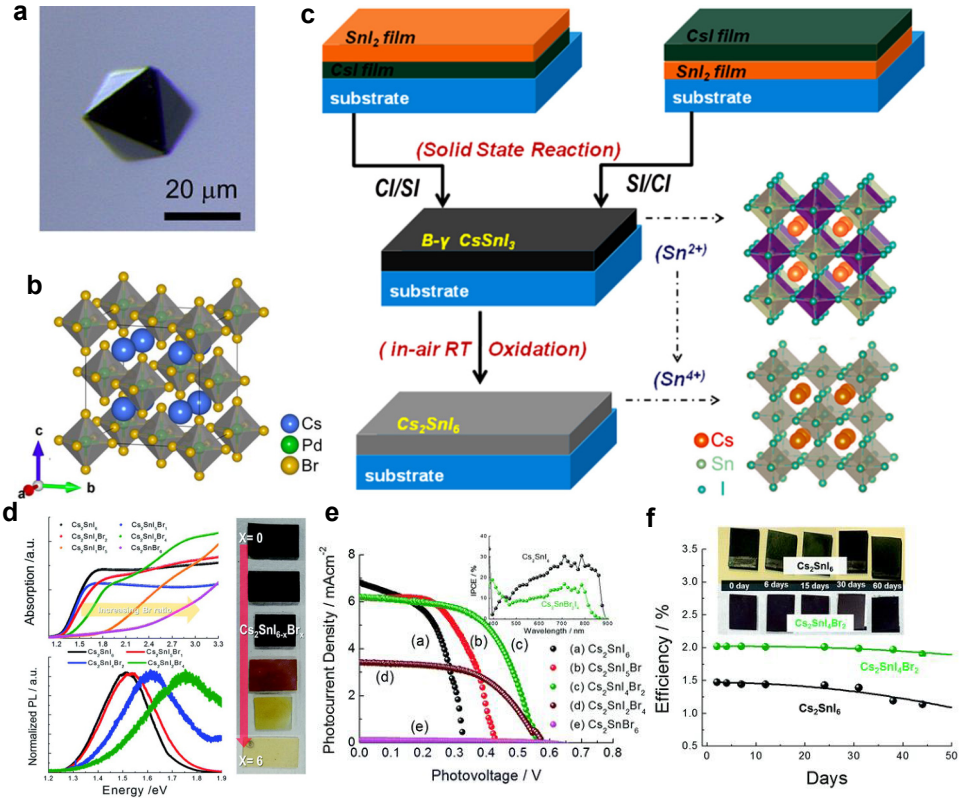

Figure 10 (a) Optical microscope image of a Cs_2PdBr_6 single crystal. (b) 3D crystal structure of Cs_2PdBr_6 showing the unit cell. Reproduced with permission from Ref. [103] ©2017, American Chemical Society. (c) Schematic of Cs_2SnI_6 film growth from $CsSnI_3$ via a two-step deposition method based on solid-state reaction, with the perovskite crystal structures of Cs_2SnI_6 and $CsSnI_3$ also shown. Reproduced with permission from Ref. [105] ©2016 Elsevier B.V. (d) Absorption spectra and photoluminescence (PL) analysis of various $Cs_2SnI_{6-x}Br_x$ compositions prepared using the two-step solution process. (e) *J*–*V* characteristic curves of a series of "sandwich"-type cells with varying compositions of $Cs_2SnI_{6-x}Br_x$, with the inset showing the IPCE values for Cs_2SnI_6 (black) and $Cs_2SnBr_2I_4$ (green). (f) Stability curves for 50 d for Cs_2SnI_6 (black) and the $Cs_2SnBr_2I_4$ (green)-based solar cells. Reproduced with permission from Ref. [106] ©2017, The Royal Society of Chemistry.

to 2.9 eV through halide mixing in Cs_2SnX_6 (X = I/Br)[105,106]. Figure 10d shows that Cs_2SnBr_6 exhibits a bandgap of 2.9 eV, significantly higher than that of Cs_2SnI_6 (1.3 eV). Increasing Br content in $Cs_2SnBr_xI_{6-x}$ films shifts their color from dark brown to brown/red and ultimately to light yellow, reflecting the widening bandgap. Owing to its narrow bandgap, Cs_2SnI_6 is a promising light absorber for solar cells and can be prepared via a two-step solution process[106] or derived from $CsSnI_3$ through controlled air oxidation[105]. Solar cells based on Cs_2SnI_6 and $Cs_2SnI_{6-x}Br_x$ absorbers have achieved PCEs of 0.96% and 2.025%, respectively (Fig. 10e). Among these, $Cs_2SnI_4Br_2$ shows the best performance, with markedly enhanced stability compared to Cs_2SnI_6 (Fig. 10f). Despite the diverse substitution strategies available in other metal-based lead-free perovskites, significant challenges remain in achieving high efficiency and long-term stability.

Other metal-based PSCs represent a critical pathway toward fully lead-free solar cells, offering opportunities for material diversification and structural innovation. However, their development faces significant challenges. These materials generally exhibit low power conversion efficiencies, often below 4%, limiting their competitiveness with Pb-based or Sn–Pb hybrid systems. Ge-based perovskites, despite having suitable bandgaps, suffer from facile Ge^{2+} oxidation and difficulties in achieving high-quality thin films. Bi- and Sb-based $A_3B_2X_9$ compounds typically have wide bandgaps (>2 eV), restricted light absorption ranges, and high exciton binding energies or indirect bandgaps, which impede efficient charge generation and extraction. Similarly, double perovskites ($A_2B^{4+}X_6$) are constrained by low carrier mobility, weak light absorption, and forbidden electronic transitions. Beyond their wide bandgaps and low carrier mobility, the limited performance of other metal-based perovskites stems largely from their intrinsic electronic structures. In Bi- and Sb-based low-dimensional (0D/2D) systems, strong structural confinement produces highly localized electronic states and large carrier effective masses, which severely hinder charge transport[107]. Unlike Pb- and Sn-based perovskites, which exhibit defect tolerance due to antibonding valence band maxima and strong spin–orbit coupling, Bi/Sb-based systems generally lack this feature, leading to deep trap states and pronounced nonradiative recombination[108]. Additionally, these materials require systematic optimization of environmental stability, interfacial compatibility, and reproducible fabrication methods.

Despite their currently low efficiency, other metal-based perovskites offer notable advantages in environmental compatibility, structural stability, and bandgap tunability.

They are particularly suited for specialized optoelectronic applications, such as low-light energy harvesting and radiation detection. A summary of the photovoltaic performance of other metal-based PSCs is presented in Table 3 . Future research should explore novel B-site cation combinations and structural designs using theoretical modeling and high-throughput screening. Approaches such as mixed-valence states, dimensional engineering, and heterostructure formation can optimize band structures, enhance light absorption, and improve charge transport. Additionally, advancements in interface engineering, defect passivation, and low-temperature, green synthesis methods are expected to significantly boost performance and practical applicability. In the long term, these materials could enable flexible and wearable photovoltaics, as well as environmentally compatible integrated optoelectronic devices, providing an important complement to fully lead-free perovskite photovoltaic technologies.

5 Pb-free double perovskites

5.1 Group 14/14 mixed-cation double perovskites

While single- or simple mixed-B-site perovskites (e.g., Sn, Ge, Bi, Sb) have shown promise as lead-free alternatives, they remain limited by stability and performance challenges. To overcome these issues and eliminate lead toxicity, research has increasingly focused on double perovskite systems, which offer enhanced structural diversity and design flexibility. In these structures, the two Pb^{2+} ions of conventional perovskites are replaced either by two divalent cations (B'^{2+} and B''^{2+}) or by a monovalent (B'^{+}) and a trivalent cation (B''^{3+}), forming the $A_2B'B''X_6$ double perovskite framework. Representative examples include $CsGe_{0.5}Sn_{0.5}I_3$ and $Cs_2AgBiBr_6$, corresponding to Group 14/14 and Group 11/15 mixed-cation double perovskites, respectively[109,110], and are among the most widely studied members of this class. The Group 14/14 double perovskite family is exemplified by the $CsGe_{1-x}Sn_xI_3$ system, a promising lead-free perovskite alternative. First-principles calculations by Zhou et al. revealed that for x = 0.25 and 0.75, defect states are deep within the bandgap and highly localized. In contrast, at x = 0.5, singly occupied defect states become more delocalized and energetically shallower, as illustrated in Figs. 11a–11c. In this analysis, one defect state occupied by a single electron is denoted occ1, while a second state occupied by two electrons is denoted occ2. This trend is attributed to variations in orbital hybridization between the defective Ge atom and its neighboring cations. At x = 0.5, weaker hybridization raises the energy of the occ1 state[109]. For x = 0.25 and 0.75, the deep-level occ1 states primarily arise from the bonding interactions between Ge_D 4p orbitals and the p orbitals of adjacent Ge_{NN}/Sn_{NN} atoms, as shown by partial charge densities (Fig. 11d) and crystal orbital Hamilton population (COHP) analysis (Figs. 11a and 11c). In general, stronger orbital hybridization corresponds to lower-energy bonding states (Fig. 11e). For $CsGe_{1-x}Sn_xI_3$, the average bond length between Ge_D and neighboring Ge_{NN}/Sn_{NN} atoms is larger at x = 0.5 than at x = 0.25 and 0.75 (Fig. 11d), indicating weaker hybridization and a correspondingly higher-energy occ1 state in $CsGe_{0.5}Sn_{0.5}I_3$. These results underscore the critical role of compositional alloying in modulating defect-state characteristics. Specifically, the $CsGe_{0.5}Sn_{0.5}I_3$ composition effectively mitigates the detrimental effects of SnI and GeI antisite defects, highlighting alloy engineering as a promising strategy to enhance material properties and advance high-performance, lead-free perovskite devices.

5.2 Group 11/15 mixed-cation double perovskite

Among Group 11/15 mixed-cation double perovskites, $Cs_2AgBiBr_6$ has emerged as a leading candidate. For instance, $Cs_2AgBiBr_6$ solar cells processed under high-temperature annealing exhibited energy levels as shown in Fig. 12a and achieved a PCE of 2.43% with a V_{oc} of 0.98 V[111]. High-quality $Cs_2AgBiBr_6$ films were also fabricated via a low-pressure-assisted solution process under ambient conditions (Figs. 12b and 12c), yielding planar heterojunction solar cells with a maximum PCE of 1.44%[112]. Moreover, the efficiency and stability of Bi-halide double PSCs were enhanced through synergistic interface engineering of the ETL/HTL[113]. Specifically, modifying the TiO_2 ETL with a hydrophobic C_{60} interlayer and replacing the lithium-doped small-molecule HTL with an undoped conjugated polymer improved perovskite surface quality and optimized energy-level alignment at the contacts (Fig. 12d). Consequently, the

Table 3 Key photovoltaic performance metrics of representative other metal-based PSCs

Type	Device structure	V_{oc} (V)	J_{sc} (mA cm^{-2})	FF (%)	PCE (%)	Ref.
$AB^{2+}X_3$ perovskite	FTO/c-TiO_2/mp-TiO_2/$CsGeI_3$/spiro-OMeTAD/Au	0.074	5.7	27	0.11	79
	FTO/c-TiO_2/mp-TiO_2/$MAGeI_3$/spiro-OMeTAD/Au	0.15	4.0	30	0.2	79
	ITO/PEDOT:PSS/$MAGeI_{2.7}Br_{0.3}$/$PC_{70}BM$/Ag	0.46	2.43	51	0.57	83
	FTO/c-TiO_2/mp-TiO_2/$Cs_3Bi_2I_9$/spiro-OMeTAD/Ag	0.85	2.15	60	1.09	91
	FTO/c-TiO_2/mp-TiO_2/$(CH_3NH_3)_3Bi_2I_9$/P3HT/Au	0.354	1.157	46.4	0.19	92
	FTO/c-TiO_2/mp-TiO_2/$(CH_3NH_3)_3Bi_2I_9$/spiro-OMeTAD/MoO_3/Ag	0.67	1	62.48	0.42	93
$A_3B^{3+}{}_2X_9$ perovskite	FTO/c-TiO_2/mp-TiO_2/$Cs_3Bi_2I_9$-$Ag_3Bi_2I_9$/PDBD-T/Au	0.78	7.65	60.12	3.59	95
	FTO/c-TiO_2/mp-TiO_2/$Cs_3Bi_2I_9$/C	1.01	3.6	77	2.81	96
	FTO/c-TiO_2/mp-TiO_2/$AgBi_2I_7$/P3HT/Au	0.56	3.3	67.41	1.22	98
	FTO/Nb_2O_5/$Cs_3Sb_2Cl_xI_{9-x}$/P3HT/C	0.84	4.47	55.13	2.07	99
$A_2B^{4+}X_6$ perovskite	FTO/c-TiO_2/mp-TiO_2/Cs_2SnI_6/P3HT/Ag	0.51	5.41	35	0.96	104
	FTO/c-TiO_2/mp-TiO_2/$Cs_2SnI_4Br_2$/Cs_2SnI_6/LPAH/FTO	0.563	6.225	57.7	2.025	105

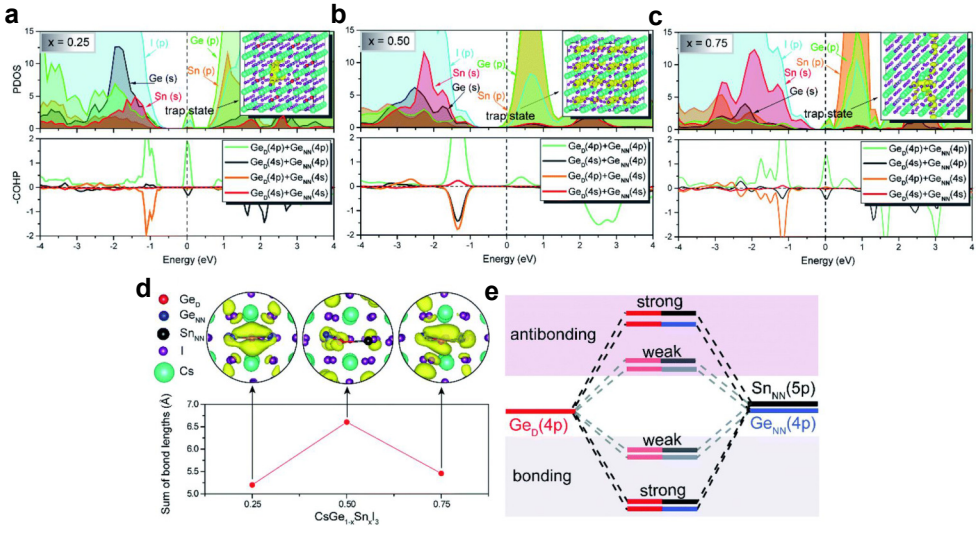

Figure 11 (a–c) Orbital-projected density of states (DOS) and projected COHP for Ge_I defects in $CsGe_{0.75}Sn_{0.25}I_3$ (x = 0.25, a), $CsGe_{0.5}Sn_{0.5}I_3$ (x = 0.50, b), and $CsGe_{0.25}Sn_{0.75}I_3$ (x = 0.75, c). The Fermi level is set to zero. Insets in the upper-right corners of the DOS panels show partial charge densities of the trap states. In the COHP plots, Ge_D denotes the defective Ge atom, and Ge_{NN} refers to the nearest neighboring Ge atom. (d) Local structures and partial charge densities surrounding Ge_D are highlighted by circles (top panel). The bottom panel shows the sum of bond lengths between Ge_D and its two nearest Ge_{NN}/Sn_{NN} neighbors. (e) Schematic illustrating how orbital hybridization strength influences the energy of hybrid orbitals. Reproduced with permission from Ref. [109] ©2021, The Royal Society of Chemistry.

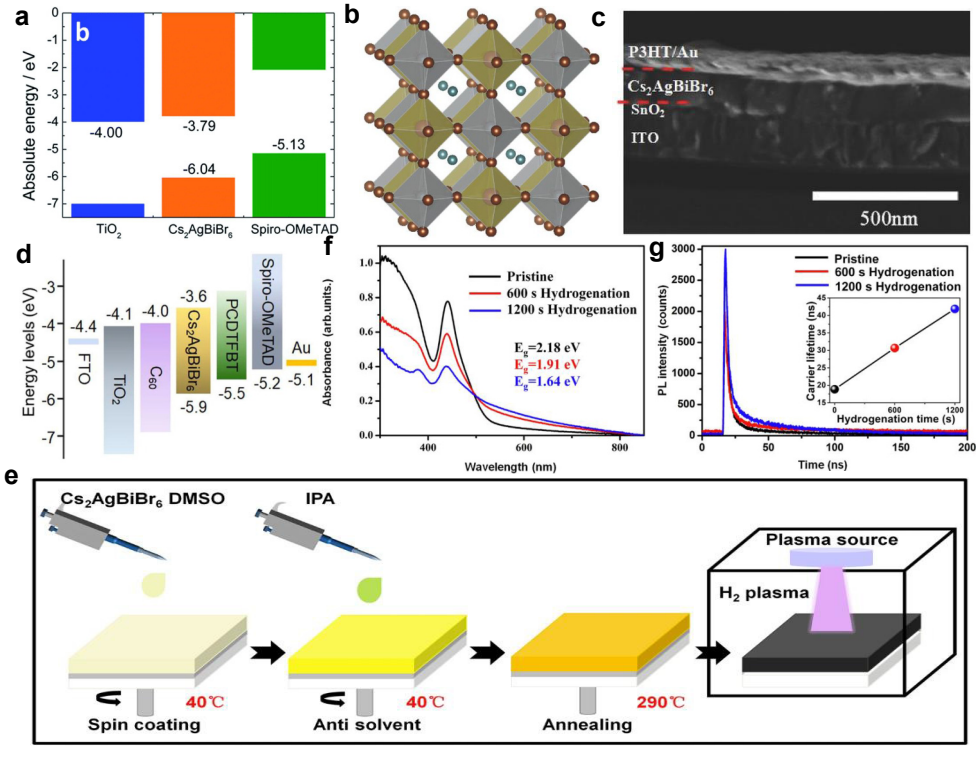

Figure 12 (a) Energy levels of the $Cs_2AgBiBr_6$ double perovskite and corresponding charge extraction materials. Reproduced with permission from Ref. [111] ©2017, The Royal Society of Chemistry. (b) Crystal structure of $Cs_2AgBiBr_6$. Br ions in deep red, Cs^+ ions in turquoise, and Ag/Bi octahedra in gray/brown polyhedral. (c) Cross-sectional SEM image of the device. Reproduced under the CC BY 4.0 license from Ref. [112] ©2017, The Authors. (d) Energy-level alignment within the PSC. Reproduced with permission from Ref. [113] ©2020, Science Press and Dalian Institute of Chemical Physics, Chinese Academy of Sciences. (e) Preparation method for $Cs_2AgBiBr_6$ thin films. (f) UV–vis absorption spectra of $Cs_2AgBiBr_6$ films under varying hydrogenation times. (g) Time-resolved photoluminescence and carrier lifetime measurements for $Cs_2AgBiBr_6$ films with different hydrogenation durations. Reproduced under the CC BY 4.0 license from Ref. [114] ©2022, The Authors.

optimized $Cs_2AgBiBr_6$ devices exhibited reduced trap densities, suppressed charge recombination, and enhanced charge extraction, resulting in a 69% efficiency improvement and a PCE of 1.57% compared to the control. Zhang et al. applied a hydrogenation treatment (Fig. 12e) to tune the bandgap of $Cs_2AgBiBr_6$ films from 2.18 to 1.64 eV (Fig. 12f). The hydrogenated films achieved a PCE of 6.37%[114], representing the highest efficiency reported for double PSCs to date, while maintaining good environmental stability. Subsequent analyses confirmed that atomic hydrogen doping modifies the valence and conduction band positions and enhances both carrier mobility and lifetime (Fig. 12g). Recently, Mo-doped $Cs_2AgBiBr_6$ lead-free halide double perovskite films, prepared via a sol-gel method, demonstrated enlarged grain size and a reduced bandgap of 1.86 eV. Solar cells based on these films achieved a J_{sc} of 5.59 mA cm^2, a fill factor of 0.755, V_{oc} of 0.936 V, and a PCE of 3.95%[115]. Although double perovskites offer promise for lead-free applications through multi-metal synergistic strategies, their inherently wide bandgaps and parity-forbidden transitions result in poor light absorption. Consequently, reported double perovskite devices exhibit low J_{sc} values, limiting their potential for high-efficiency performance. The performance of representative Pb-free double perovskite solar cells is summarized in Table 4 .

Despite their unique advantages in structural diversity and environmental stability, lead-free double perovskites face significant bottlenecks in photovoltaic applications. Their performance is fundamentally limited by intrinsic material properties, particularly their wide bandgaps and parity-forbidden optical transitions, which lead to weak light absorption and low short-circuit current densities. Consequently, certified PCEs for double PSCs remain in the single-digit range (~6%–7%), far below those of Pb-based and Sn–Pb hybrid systems. Nevertheless, double perovskites remain promising candidates for fully lead-free, high-performance photovoltaics due to their highly designable structures, tunable compositions, and excellent air and thermal stability. With interdisciplinary approaches and precise control over their properties, these materials hold potential for breakthroughs in targeted applications, paving the way toward stable, fully lead-free perovskite optoelectronic devices.

6 Conclusion

Lead-free PSCs have emerged as a promising, environmentally friendly, and cost-effective photovoltaic technology, demonstrating significant advances in material design, device performance, and sustainability. This review has summarized recent progress in Sn-based, hybrid Sn–Pb, and fully lead-free PSCs, highlighting both their potential and remaining challenges. While Pb-based perovskites continue to dominate due to their high efficiency, concerns over toxicity and environmental impact have accelerated the development of lead-free alternatives. Among these, Sn-based perovskites are particularly promising for their environmental benefits; however, their practical adoption is limited by poor stability, Sn^{2+} oxidation, and suboptimal charge transport. Parallel efforts in lead-free double perovskites offer a viable route to non-toxic, structurally stable materials. Although the efficiencies of these systems remain below those of Pb-based PSCs, advances in defect passivation, bandgap tuning, and interface engineering are progressively addressing these limitations, paving the way for the commercialization of high-performance, environmentally benign perovskite photovoltaics.

Despite these advancements, commercialization remains constrained by several critical challenges. Notably, the high efficiency and stability milestones cited in this review, such as 17.89% for Sn-based devices and 28.86% for tandem cells, were achieved primarily under optimized laboratory conditions. These conditions typically involved small device areas (≤0.1 cm^2), fabrication in inert atmospheres, and stability testing in controlled environments, including nitrogen-filled chambers or encapsulated cells under continuous illumination. While these results are scientifically significant and underscore the potential of lead-free perovskites, they do not fully represent performance under real-world operating conditions. Achieving long-term operational stability remains a major challenge, as current lead-free devices often degrade within hundreds of hours under light exposure or humid environments, falling far short of the ~25-year lifespan required for grid-scale deployment. The trade-off between stability and efficiency remains pronounced: while low-dimensional structures improve moisture resistance, they often hinder charge transport and reduce overall device performance. Scalable manufacturing further complicates this issue, as laboratory-scale spin-coating methods are difficult to adapt to industrial processes such as roll-to-roll or slot-die coating. Reportedly, efficiency declines by over 8% in absolute terms when scaling from small-area cells (≤ 0.1 cm^2) to large-area modules (>100 cm^2). Additionally, even in low-lead Sn–Pb systems, potential lead leakage remains a concern, as the release of lead ions from damaged modules poses environmental risks, highlighting the need for robust encapsulation strategies.

Realizing the full potential of environmentally friendly, cost-effective lead-free PSCs requires a multi-pronged approach. Materials engineering is critical for enhancing stability, efficiency, and scalability, while innovations in device architecture are essential to improve charge collection and suppress recombination losses. Strategies such as

Table 4 Performances of Pb-free double perovskites

Type	Device structure	V_{oc} (V)	J_{sc} (mA cm^{-2})	FF (%)	PCE (%)	Ref.
Pb-free double perovskite	FTO/c-TiO_2/mp-TiO_2/$Cs_2AgBiBr_6$/spiro-OMeTAD/Au	0.98	3.93	63	2.43	111
	ITO/SnO_2/$Cs_2AgBiBr_6$/P3HT/Au	1.04	1.78	78	1.44	112
	FTO/TiO_2/C_{60}/$Cs_2AgBiBr_6$/PCDTFBT/Au	1.01	2.25	69.3	1.57	113
	ITO/SnO_2/$Cs_2AgBiBr_6$/spiro-OMeTAD/Au	0.92	11.4	60.93	6.37	114
	FTO/TiO_2/$Cs_2AgBiBr_6$/spiro-OMeTAD/Au	0.936	5.59	75.5	3.95	115

additive incorporation, compositional tuning, and surface modification are expected to significantly boost performance. Robust encapsulation and packaging are also crucial to protect devices from moisture and oxygen, prolong operational lifespan, and minimize environmental risks from metal ion release. Advances in low-cost manufacturing, including roll-to-roll processing, will facilitate large-scale production and commercialization. Beyond terrestrial applications, lead-free PSCs are promising for space photovoltaics due to their lightweight nature and tunable bandgaps; assessing radiation tolerance and environmental stability could open new opportunities in extraterrestrial environments. Future research should prioritize intrinsically oxidation-resistant compositions, effective defect management, and scalable deposition techniques compatible with large-area modules. Addressing these challenges is essential to translate laboratory-scale efficiency gains into practical, commercially viable photovoltaic technologies.

Integrating lead-free perovskites into tandem solar cells offers a promising pathway to enhance efficiency and narrow the performance gap with Pb-based perovskites. Over the long term, such devices are expected to provide cost-effective, high-performance solar energy solutions while prioritizing sustainable and non-toxic materials, ultimately supporting global carbon neutrality objectives.

Acknowledgements

None.

Author contribution statement

Changkai Huang was responsible for writing – original draft, review & editing, and investigation. Yihuai Huang, Qiannan Zhao, and Zhenxuan Liu contributed to data curation and literature collection. Guibin Shen, Qinghui Jiang, and Yubo Luo were involved in writing – review & editing and formal analysis. Xin Li was responsible for conceptualization, as well as writing – review & editing. Junyou Yang provided supervision and project leadership throughout the entire process. All the authors have approved the final manuscript.

Data availability

Not applicable.

Declaration of competing interest

All the contributing authors report no conflicts of interest in this work.

Funding

This work was supported by the National Natural Science Foundation of China (Grant No. 62304082), Guangdong Basic and Applied Basic Research Foundation (Grant No. 2024A1515110044).

Use of AI statement

None.

References

[1] Kojima, A., Teshima, K., Shirai, Y., Miyasaka, T. (2009). Organometal halide perovskites as visible-light sensitizers for photovoltaic cells. *J. Am. Chem. Soc.* 131, 6050–6051,

[2] Liu, S. W., Li, J. B., Xiao, W. S., Chen, R., Sun, Z. X., Zhang, Y., Lei, X., Hu, S. F., Kober-Czerny, M., Wang, J. N., et al. (2024). Buried interface molecular hybrid for inverted perovskite solar cells. *Nature* 632, 536–542,

[3] Lin, H., Yang, M., Ru, X. N., Wang, G. S., Yin, S., Peng, F. G., Hong, C. J., Qu, M. H., Lu, J. X., Fang, L., et al. (2023). Silicon heterojunction solar cells with up to 26.81% efficiency achieved by electrically optimized nanocrystalline-silicon hole contact layers. *Nat. Energy* 8, 789–799,

[4] Jeong, J., Kim, M., Seo, J., Lu, H. Z., Ahlawat, P., Mishra, A., Yang, Y. G., Hope, M. A., Eickemeyer, F. T., Kim, M., et al. (2021). Pseudo-halide anion engineering for α-$FAPbI_3$ perovskite solar cells. *Nature* 592, 381–385,

[5] Zhang, R. K., Li, L. C., Wang, W. R., Wu, Z. J., Wang, Y., Hong, J., Rao, H. S., Pan, Z. X., Zhong, X. H. (2023). Pure-iodide wide-bandgap perovskites for high-efficiency solar cells by crystallization control. *Adv. Funct. Mater.* 33, 2300552,

[6] Montoya, M. P., Sidhik, S., Esparza, D., López-Luke, T., Zarazua, I., Rivas, J. M., De La Rosa, E. (2019). Study of inverted planar $CH_3NH_3PbI_3$ perovskite solar cells fabricated under environmental conditions. *Sol. Energy* 180, 594–600,

[7] Montoya De Los Santos, I., Cortina-Marrero, H. J., Ruíz-Sánchez, M. A., Hechavarría-Difur, L., Sánchez-Rodríguez, F. J., Courel, M., Hu, H. L. (2020). Optimization of $CH_3NH_3PbI_3$ perovskite solar cells: a theoretical and experimental study. *Sol. Energy* 199, 198–205,

[8] Yao, Z. B., Wang, W. L., Shen, H. P., Zhang, Y., Luo, Q., Yin, X. W., Dai, X. Z., Li, J. B., Lin, H. (2017). $CH_3NH_3PbI_3$ grain growth and interfacial properties in meso-structured perovskite solar cells fabricated by two-step deposition. *Sci. Technol. Adv. Mater.* 18, 253–262,

[9] Zheng, Y. F., Su, R., Xu, Z. J., Luo, D. Y., Dong, H., Jiao, B., Wu, Z. X., Gong, Q. H., Zhu, R. (2019). Perovskite solar cell towards lower toxicity: a theoretical study of physical lead reduction strategy. *Sci. Bull.* 64, 1255–1261,

[10] Noel, N. K., Stranks, S. D., Abate, A., Wehrenfennig, C., Guarnera, S., Haghighirad, A. A., Sadhanala, A., Eperon, G. E., Pathak, S. K., Johnston, M. B., et al. (2014). Lead-free organic-inorganic tin halide perovskites for photovoltaic applications. *Energy Environ. Sci.* 7, 3061–3068,

[11] Hao, F., Stoumpos, C. C., Cao, D. H., Chang, R. P. H., Kanatzidis, M. G. (2014). Lead-free solid-state organic-inorganic halide perovskite solar cells. *Nat. Photonics* 8, 489–494,

[12] Ke, W. J., Stoumpos, C. C., Kanatzidis, M. G. (2019). "Unleaded" perovskites: status quo and future prospects of tin-based perovskite solar cells. *Adv. Mater.* 31, 1803230,

[13] Park, S. W., Heo, J. H., Lee, H. J., Kim, H., Im, S. H., Hong, K. H. (2023). Compositional design for high-efficiency all-inorganic tin halide perovskite solar cells. *ACS Energy Lett.* 8, 5061–5069,

[14] Li, P. Z., Cao, X. R., Li, J. R., Jiao, B., Hou, X., Hao, F., Ning, Z. J., Bian, Z. Q.,Xi, J., Ding, L. M., et al. (2023). Ligand engineering in tin-based perovskite solar cells. *Nano-Micro Lett.* 15, 167,

[15] Lv, S. S., Gao, W. Y., Ran, C. X., Li, D. L., Chao, L. F., Wang, X. B., Song, L., Lin, Z. Q., Fu, L., Chen, Y. H. (2021). Antisolvent-free fabrication of efficient and stable Sn-Pb perovskite solar cells. *Sol. RRL* 5, 2100675,

[16] Hu, S., Otsuka, K., Murdey, R., et al. (2022). Optimized carrier extraction at interfaces for 23.6% efficient tin-lead perovskite solar cells. *Energy Environ. Sci.* 15, 2096–2107,

[17] Hamukwaya, S. L., Hao, H. Y., Mashingaidze, M. M., Zhong, T. T., Tang, S., Dong, J. J., Xing, J., Liu, H. (2022). Potassium iodide-modified lead-free $Cs_3Bi_2I_9$ perovskites for enhanced high-efficiency solar cells. *Nanomaterials* 12, 3751,

[18] Volonakis, G., Filip, M. R., Haghighirad, A. A., Sakai, N., Wenger, B., Snaith, H. J., Giustino, F. (2016). Lead-free halide double perovskites via heterovalent substitution of noble metals. *J. Phys. Chem. Lett.* 7, 1254–1259,

[19] Hao, F., Stoumpos, C. C., Guo, P. J., Zhou, N. J., Marks, T. J., Chang, R. P. H., Kanatzidis, M. G. (2015). Solvent-mediated crystallization of $CH_3NH_3SnI_3$ films for heterojunction depleted perovskite solar cells. *J. Am. Chem. Soc.* 137, 11445–11452,

[20] Weiss, M., Horn, J., Richter, C., Schlettwein, D. (2016). Preparation and characterization of methylammonium tin iodide layers as photovoltaic absorbers. *Phys. Status Solidi A Appl. Mater. Sci.* 213, 975–981,

[21] Jung, M. C., Raga, S. R., Qi, Y. B. (2016). Properties and solar cell applications of Pb-free perovskite films formed by vapor deposition. *RSC Adv.* 6, 2819–2825,

[22] Koh, T. M., Krishnamoorthy, T., Yantara, N., Shi, C., Leong, W. L., Boix, P. P., Grimsdale, A. C., Mhaisalkar, S. G., Mathews, N. (2015). Formamidinium tin-based perovskite with low E_g for photovoltaic applications. *J. Mater. Chem. A* 3, 14996–15000,

[23] Stoumpos, C. C., Malliakas, C. D., Kanatzidis, M. G. (2013). Semiconducting tin and lead iodide perovskites with organic cations: phase transitions, high mobilities, and near-infrared photoluminescent properties. *Inorg. Chem.* 52, 9019–9038,

[24] Dang, Y. Y., Zhou, Y. A., Liu, X. L., Ju, D. X., Xia, S. Q., Xia, H. B., Tao, X. T. (2016). Formation of hybrid perovskite tin iodide single crystals by top-seeded solution growth. *Angew. Chem. Int. Ed.* 55, 3447–3450,

[25] Wang, F., Ma, J. L., Xie, F. Y., Li, L. K., Chen, J., Fan, J., Zhao, N. (2016). Organic cation-dependent degradation mechanism of organotin halide perovskites. *Adv. Funct. Mater.* 26, 3417–3423,

[26] Lee, S. J., Shin, S. S., Kim, Y. C., Kim, D., Ahn, T. K., Noh, J. H., Seo, J., Seok, S. I. (2016). Fabrication of efficient formamidinium tin iodide perovskite solar cells through SnF_2-pyrazine complex. *J. Am. Chem. Soc.* 138, 3974–3977,

[27] Liao, W. Q., Zhao, D. W., Yu, Y., Grice, C. R., Wang, C. L., Cimaroli, A. J., Schulz, P., Meng, W. W., Zhu, K., Xiong, R. G., et al. (2016). Lead-free inverted planar formamidinium tin triiodide perovskite solar cells achieving power conversion efficiencies up to 6.22%. *Adv. Mater.* 28, 9333–9340,

[28] Ke, W. J., Stoumpos, C. C., Spanopoulos, I., Mao, L. L., Chen, M., Wasielewski, M. R., Kanatzidis, M. G. (2017). Efficient lead-free solar cells based on hollow {en}$MaSnI_3$ perovskites. *J. Am. Chem. Soc.* 139, 14800–14806,

[29] Yang, W. S., Park, B. W., Jung, E. H., Jeon, N. J., Kim, Y. C., Lee, D. U., Shin, S. S., Seo, J., Kim, E. K., Noh, J. H., et al. (2017). Iodide management in formamidinium-lead-halide-based perovskite layers for efficient solar cells. *Science* 356, 1376–1379,

[30] Jeon, N. J., Noh, J. H., Yang, W. S., Kim, Y. C., Ryu, S., Seo, J., Seok, S. I. (2015). Compositional engineering of perovskite materials for high-performance solar cells. *Nature* 517, 476–480,

[31] Liu, X., Yang, Z. B., Chueh, C. C., Rajagopal, A., Williams, S. T., Sun, Y., Jen, A. K. Y. (2016). Improved efficiency and stability of Pb-Sn binary perovskite solar cells by Cs substitution. *J. Mater. Chem. A* 4, 17939–17945,

[32] Zhao, Z. R., Gu, F. D., Li, Y. L., Sun, W. H., Ye, S. Y., Rao, H. X., Liu, Z. W., Bian, Z. Q., Huang, C. H. (2017). Mixed-organic-cation tin iodide for lead-free perovskite solar cells with an efficiency of 8.12%. *Adv. Sci.* 4, 1700204,

[33] Jokar, E., Chien, C. H., Tsai, C. M., Fathi, A., Diau, E. W. G. (2019). Robust tin-based perovskite solar cells with hybrid organic cations to attain efficiency approaching 10. *Adv. Mater.* 31, 1804835,

[34] Wang, L., Bi, H., Liu, J. Q., Wei, Y. Y., Zhang, Z., Chen, M. M., Baranwal, A. K., Kapil, G., Kitamura, T., Yang, S. Z., et al. (2024). Exceeding 15% performance with energy level tuning in tin-based perovskite solar cells. *ACS Energy Lett.* 9, 6238–6244,

[35] Smith, I. C., Hoke, E. T., Solis-Ibarra, D., McGehee, M. D., Karunadasa, H. I. (2024). A Layered Hybrid Perovskite Solar-Cell Absorber with Enhanced Moisture Stability. *Angew. Chem. Int. Ed.* 53, 11232–11235,

[36] Zou, Y., Gao, Y. P., Liu, Y. S. (2024). The role of organic spacers in 2D/3D hybrid perovskite solar cells. *Mater. Chem. Front.* 8, 82–103,

[37] Mao, L. L., Stoumpos, C. C., Kanatzidis, M. G. (2019). Two-dimensional hybrid halide perovskites: principles and promises. *J. Am. Chem. Soc.* 141, 1171–1190,

[38] Cao, D. H., Stoumpos, C. C., Yokoyama, T., Logsdon, J. L., Song, T. B., Farha, O. K., Wasielewski, M. R., Hupp, T., Kanatzidis, M. G. (2017). Thin films and solar cells based on semiconducting two-dimensional Ruddlesden-Popper $(CH_3(CH_2)_3NH_3)_2(CH_3NH_3)_{n-1}Sn_nI_{3n+1}$ perovskites. *ACS Energy Lett.* 2, 982–990,

[39] Liao, Y. Q., Liu, H. F., Zhou, W. J., Yang, D. W., Shang, Y. Q., Shi, Z. F., Li, B. H., Jiang, X. Y., Zhang, L. J., Quan, L. N., et al. (2017). Highly oriented low-dimensional tin halide perovskites with enhanced stability and photovoltaic performance. *J. Am. Chem. Soc.* 139, 6693–6699,

[40] Li, F. M., Xie, Y. R., Hu, Y. C., Long, M. Z., Zhang, Y. F., Xu, J. B., Qin, M. C., Lu, X. H., Liu, M. Z. (2020). Effects of alkyl chain length on crystal growth and oxidation process of two-dimensional tin halide perovskites. *ACS Energy Lett.* 5, 1422–1429,

[41] Park, I. H., Chu, L. Q., Leng, K., Choy, Y. F., Liu, W., Abdelwahab, I., Zhu, Z. Y., Ma, Z. R., Chen, W., Xu, Q. H., et al. (2019). Highly stable two-dimensional tin(II) iodide hybrid organic-inorganic perovskite based on stilbene derivative. *Adv. Funct. Mater.* 29, 1904810,

[42] Li, M., Zuo, W. W., Yang, Y. G., Aldamasy, M. H., Wang, Q., Cruz, S. H. T., Feng, S. L., Saliba, M., Wang, Z. K., Abate, A. (2020). Tin halide perovskite films made of highly oriented 2D crystals enable more efficient and stable lead-free perovskite solar cells. *ACS Energy Lett.* 5, 1923–1929,

[43] Yu, B. B., Chen, Z. H., Zhu, Y D., Wang, Y. Y., Han, B., Chen, G. C., Zhang, X. S., Du, Z., He, Z. B. (2021). Heterogeneous 2D/3D tin-halides perovskite solar cells with certified conversion efficiency breaking 14%. *Adv. Mater.* 33, 2102055,

[44] Chen, J. F., Luo, J. F., Li, Y. Q., Chen, X. Y., Song, Z. Y., Hou, E. L., Sun, C., Zhang, H., Cheng, S., Xing, Y. M., et al. (2025). Spatially isomeric fulleropyrrolidines enable controlled stacking of perovskite colloids for high-performance tin-based perovskite solar cells. *Angew. Chem. Int. Ed.* 64, e202420150,

[45] Li, T. P., Luo, X., Wang, P. L., Li, Z., Li, Y. M., Huang, J. H., Jin, Z. M., Yang, Y. G., Li, B., Zhang, W. Q., et al. (2025). Tin-based perovskite solar cells with a homogeneous buried interface. *Nature* 648, 84–90,

[46] Chung, I., Song, J. H., Im, J., Androulakis, J., Malliakas, C. D., Li, H., Freeman, A. J., Kenney, J. T., Kanatzidis, M. G. (2012). $CsSnI_3$: semiconductor or metal? High electrical conductivity and strong near-infrared photoluminescence from a single material. High hole mobility and phase-transitions. *J. Am. Chem. Soc.* 43, 8579–8587,

[47] Scaife, D. E., Weller, P. F., Fisher, W. G. (1974). Crystal preparation and properties of cesium tin(II) trihalides. *J. Solid State Chem.* 9, 308–314,

[48] Chen, Z., Wang, J. J., Ren, Y. H., Yu, C. L., Shum, K. (2012). Schottky solar cells based on $CsSnI_3$ thin-films. *Appl. Phys. Lett.*

101, 093901,

[49] Kumar, M. H., Dharani, S., Leong, W. L., Boix, P. P., Prabhakar, R. R., Baikie, T., Shi, C., Ding, H., Ramesh, R., Asta, M., et al. (2014). Lead-free halide perovskite solar cells with high photocurrents realized through vacancy modulation. *Adv. Mater.* 26, 7122–7127,

[50] Chung, I., Lee, B., He, J., Q., Chang, R. P. H., Kanatzidis, M. G. (2012). All-solid-state dye-sensitized solar cells with high efficiency. *Nature* 485, 486–489,

[51] Sabba, D., Mulmudi, H. K., Prabhakar, R. R., Krishnamoorthy, T., Baikie, T., Boix, P. P., Mhaisalkar, S., Mathews, N. (2015). Impact of anionic Br substitution on open circuit voltage in lead free perovskite ($CsSnI_{3-x}Br_x$) solar cells. *J. Phys. Chem. C* 119, 1763–1767,

[52] Wang, N., Zhou, Y. Y., Ju, M. G., Garces, H. F., Ding, T., Pang, S. P., Zeng, X. C., Padture, N. P., Sun, X. W., et al. (2016). Heterojunction-depleted lead-free perovskite solar cells with coarse-grained B-γ-$CsSnI_3$ thin films. *Adv. Energy Mater.* 6, 1601130,

[53] Marshall, K. P., Walker, M., Walton, R. I., Hatton, R. A. (2016). Enhanced stability and efficiency in hole-transport-layer-free $CsSnI_3$ perovskite photovoltaics. *Nat. Energy* 1, 16178,

[54] Li, B., Di, H. X., Chang, B. H., Yin, R. Y., Fu, L., Zhang, Y. N., Yin, L. W. (2021). Efficient passivation strategy on Sn related defects for high performance all-inorganic $CsSnI_3$ perovskite solar cells. *Adv. Funct. Mater.* 31, 2007447,

[55] Duan, C. H., Zou, F. L., Wen, Q. Y., Qin, M. C., Li, J., Chen, C., Lu, X. H., Ding, L. M., Yan, K. Y. (2023). A bifunctional carbazide additive for durable $CsSnI_3$ perovskite solar cells. *Adv. Mater.* 35, 2300503,

[56] Yang, Z. B., Zhang, X. H., Yang, W. Y., Eperon, G. E., Ginger, D. S. (2020). Tin-lead alloying for efficient and stable all-inorganic perovskite solar cells. *Chem. Mater.* 32, 2782–2794,

[57] Yu, H. X., Fu, L. J., Sun, T. Y., Wang, D. Y., Liu, Z. R., Huang, J. Y., Zhang, Z. G., Ma, X. T., Li, X. J., Hu, B., et al. (2025). Modulation of electron transport layers to minimize voltage loss in $CsSnI_3$ perovskite solar cells. *ACS Energy Lett.* 10, 2889–2897,

[58] Zhang, M., Lyu, M. Q., Yun, J. H., Noori, M., Zhou, X. J., Cooling, N. A., Wang, Q., Yu, H., Dastoor, P. C., Wang, L. Z. (2016). Low-temperature processed solar cells with formamidinium tin halide perovskite/fullerene heterojunctions. *Nano Res.* 9, 1570–1577,

[59] Yang, Y., Chen, R. H., Wu, J. D., Dai, Z. Y., Luo, C. Y., Fang, Z. Y., Wan, S. Y., Chao, L. F., Liu, Z., Wang, H. Q. (2024). Bilateral chemical linking at NiO_x buried interface enables efficient and stable inverted perovskite solar cells and modules. *Angew. Chem. Int. Ed.* 63, e202409689,

[60] Yang, Y., Chen, S. Y., Dai, Z. Y., Wei, H., Wan, S. Y., Chen, Y., Sun, J. H., Liu, Z., Ding, L. M., Xia, H. P., et al. (2025). Bridged carbolong modulating interfacial charge transfer enhancement for high-performance inverted perovskite solar cells. *Angew. Chem. Int. Ed.* 64, e202420262,

[61] Ogomi, Y., Morita, A., Tsukamoto, S., Saitho, T., Fujikawa, N., Shen, Q., Toyoda, T., Yoshino, K., Pandey, S. S., Ma, T. L., et al. (2014). $CH_3NH_3Sn_xPb_{(1-x)}I_3$ perovskite solar cells covering up to 1060 nm. *J. Phys. Chem. Lett.* 5, 1004–1011,

[62] Im, J., Stoumpos, C. C., Jin, H., Freeman, A. J., Kanatzidis, M. G. (2015). Antagonism between spin-orbit coupling and steric effects causes anomalous band gap evolution in the perovskite photovoltaic materials $CH_3NH_3Sn_{1-x}Pb_xI_3$. *J. Phys. Chem. Lett.* 6, 3503–3509,

[63] Chang, S., Zhang, Z., Su, Y. T., Yao, S., Yang, Y. X., Yang, Z., Wang, A. F., Cao, J. P., Huang, W., Dong, J. J., et al. (2024). Synergetic effect of non-invasive posttreatment agents enables highly efficient and stable all-inorganic Sn-Pb perovskite solar cells. *Chem. Eng. J.* 500, 156707,

[64] Zuo, F., Williams, S. T., Liang, P. W., Chueh, C. C., Liao, C. Y., Jen, A, K. Y. (2014). Binary-metal perovskites toward high-performance planar-heterojunction hybrid solar cells. *Adv. Mater.* 26, 6454–6460,

[65] Zhu, H. L., Xiao, J. Y., Mao, J., Zhang, H., Zhao, Y., Choy, W. C. H. (2017). Controllable crystallization of $CH_3NH_3Sn_{0.25}Pb_{0.75}I_3$ perovskites for hysteresis-free solar cells with efficiency reaching 15.2%. *Adv. Funct. Mater.* 27, 1605469,

[66] Zong, Y. X., Zhou, Z. M., Chen, M., Padture, N. P., Zhou, Y. Y. (2018). Lewis-adduct mediated grain-boundary functionalization for efficient ideal-bandgap perovskite solar cells with superior stability. *Adv. Energy Mater.* 8, 1800997,

[67] Zhu, Z. L., Li, N., Zhao, D. B., Wang, L. D., Jen, A. K. Y. (2019). Improved efficiency and stability of Pb/Sn binary perovskite solar cells fabricated by galvanic displacement reaction. *Adv. Energy Mater.* 9, 1802774,

[68] Lin, R. X., Xiao, K., Qin, Z. Y., Han, Q. L., Zhang, C. F., Wei, M. Y., Saidaminov, M. I., Gao, Y., Xu, J., Xiao, M., et al. (2019). Monolithic all-perovskite tandem solar cells with 24.8% efficiency exploiting comproportionation to suppress Sn(II) oxidation in precursor ink. *Nat. Energy* 4, 864–873,

[69] Kapil, G., Bessho, T., Ng, C. H., Hamada, K., Pandey, M., Kamarudin, M. A., Hirotani, D., Kinoshita, T., Minemoto, T., Shen, Q., et al. (2019). Strain relaxation and light management in tin-lead perovskite solar cells to achieve high efficiencies. *ACS Energy Lett.* 4, 1991–1998,

[70] Hu, M. Y., Chen, M., Guo, P. J., Zhou, H., Deng, J. J., Yao, Y. D., Jiang, Y., Gong, J., Dai, Z. H., Zhou, Y. X., et al. (2020). Sub-1.4eV bandgap inorganic perovskite solar cells with long-term stability. *Nat. Commun.* 11, 151,

[71] Zhang, Y., Li, C. Y., Zhao, H. Y., Yu, Z. X., Tang, X. A., Zhang, J. X., Chen, Z. H., Zeng, J. R., Zhang, P., Han, L. Y., et al. (2024). Synchronized crystallization in tin-lead perovskite solar cells. *Nat. Commun.* 15, 6887,

[72] Yuan, C. J., Chen, M. Q., Wang, D., Zeng, J., Wang, J. R., Huang, X. F., Liu, K. K., Shen, T., Lei, X., Yue, Z. Y., et al. (2025). Redox shuttle-stabilized tin-lead perovskites for all-perovskite tandem solar cells. *ACS Energy Lett.* 10, 4749–4757,

[73] Eperon, G. E., Hörantner, M. T., Snaith, H. J. (2017). Metal halide perovskite tandem and multiple-junction photovoltaics. *Nat. Rev. Chem.* 1, 0095,

[74] Leijtens, T., Bush, K. A., Prasanna, R., McGehee, M. D. (2018). Opportunities and challenges for tandem solar cells using metal halide perovskite semiconductors. *Nat. Energy* 3, 828–838,

[75] Eperon, G. E., Leijtens, T., Bush, K. A., Prasanna, R., Green, T., Wang, J. T. W., Mcmeekin, D. P., Volonakis, G., Milot, R. L., May, R., et al. (2016). Perovskite-perovskite tandem photovoltaics with optimized band gaps. *Science* 354, 861–865,

[76] Palmstrom, A. F., Eperon, G. E., Leijtens, T., Prasanna, R., Habisreutinger, S. N., Nemeth, W., Gaulding, E. A., Dunfield, S. P., Reese, M., Nanayakkara, S., et al. (2019). Enabling flexible all-perovskite tandem solar cells. *Joule* 3, 2193–2204,

[77] Ma, T. S., Wang, H. Y., Wu, Z. H., Zhao, Y., Chen, C., Yin, X. X., Hu, L., Yao, F., Lin, Q. Q., Wang, S. J., et al. (2024). Hole transport layer-free low-bandgap perovskite solar cells for efficient all-perovskite tandems. *Adv. Mater.* 36, 2308240,

[78] Pan, Y. Y., Wang, J. N., Sun, Z. X., Zhang, J. Q., Zhou, Z., Shi, C. Y., Liu, S. W., Ren, F. M., Chen, R., Cai, Y., et al. (2024). Surface chemical polishing and passivation minimize non-radiative recombination for all-perovskite tandem solar cells. *Nat. Commun.* 15, 7335,

[79] Sun, P. P., Li, Q. S., Yang, L. N., Li, Z. X. (2016). Theoretical

insights into a potential lead-free hybrid perovskite: substituting Pb^{2+} with Ge^{2+}. *Nanoscale* 8, 1503–1512,

[80] Krishnamoorthy, T., Ding, H., Yan, C., Leong, W. L., Baikie, T., Zhang, Z. Y., Sherburne, M., Li, S. Z., Asta, M., Mathews, N., et al. (2015). Lead-free germanium iodide perovskite materials for photovoltaic applications. *J. Mater. Chem. A* 3, 23829–23832,

[81] Zhang, Y. L., Meng, X. R., Liu, X. J., Zhou, F. H., Yang, W., Fan, Y. X., He, P., Wu, J., Wang, H., Cheng, Y. H. (2023). SCAPS simulation and DFT study of lead-free perovskite solar cells based on $CsGeI_3$. *Mater. Chem. Phys.* 306, 128084,

[82] Ur Rehman, U., Ul Sahar, K., Hussain, E., Wang, C. M. (2024). Performance optimization of lead-free potassium germanium halide based perovskite solar cells: a numerical study. *Sol. Energy* 277, 112752,

[83] Lu, J. H., Chen, S., Wang, H. R., Qiu, L., Wu, C. Y., Qian, W. C., Wang, Z. J., Huang, K., Wu, J., Chen, H., et al. (2024). Replacing the electron-hole transport layer with doping: SCAPS simulation of lead-free germanium-based perovskite solar cells based on $CsGeI_3$. *Sol. Energy Mater. Sol. Cells* 271, 112883,

[84] Kopacic, I., Friesenbichler, B., Hoefler, S. F., Kunert, B., Plank, H., Rath, T., Trimmel, G. (2018). Enhanced performance of germanium halide perovskite solar cells through compositional engineering. *ACS Appl. Energy Mater.* 1, 343–347,

[85] Uribe, J. I., Ramirez, D., Osorio-Guillén, J. M., Osorio, J., Jaramillo, F. (2016). $CH_3NH_3CaI_3$ Perovskite: synthesis, characterization, and first-principles studies. *J. Phys. Chem. C* 120, 16393–16398,

[86] Pazoki, M., Jacobsson, T. J., Hagfeldt, A., Boschloo, G., Edvinsson, T. (2016). Effect of metal cation replacement on the electronic structure of metalorganic halide perovskites: replacement of lead with alkaline-earth metals. *Phys. Rev. B* 93, 144105,

[87] Filip, M. R., Giustino, F. (2016). Computational screening of homovalent lead substitution in organic-inorganic halide perovskites. *J. Phys. Chem. C* 120, 166–173,

[88] McCall, K. M., Stoumpos, C. C., Kostina, S. S., Kanatzidis, M. G., Wessels, B. W. (2017). Strong electron-phonon coupling and self-trapped excitons in the defect halide perovskites $A_3M_2I_9$ (A = Cs, Rb; M = Bi, Sb). *Chem. Mater.* 29, 4129–4145,

[89] Ghebouli, M. A., Chihi, T., Ghebouli, B., Fatmi, M. (2018). Study of the structural, elastic, electronic and optical properties of lead free halide double perovskites Cs_2AgBiX_6 (X = *Br, Cl*). *Chin. J. Phys.* 56, 323–330,

[90] Chang, J. H., Doert, T., Ruck, M. (2016). Structural variety of defect perovskite variants $M_3E_2X_9$ (M = Rb, Tl, E = Bi, Sb, X = Br, I). *Z. Anorg. Allg. Chem.* 47, 736–748,

[91] Lehner, A. J., Fabini, D. H., Evans, H. A., Hébert, C. A., Smock, S. R., Hu, J., Wang, H. B., Zwanziger, J. W., Chabinyc, M. L., Seshadri, R. (2015). Crystal and electronic structures of complex bismuth iodides $A_3Bi_2I_9$ (A = K, Rb, Cs) related to perovskite: aiding the rational design of photovoltaics. *Chem. Mater.* 27, 7137–7148,

[92] Park, B. W., Philippe, B., Zhang, X. L., Rensmo, H., Boschloo, G., Johansson, E. M. J. (2015). Bismuth based hybrid perovskites $A_3Bi_2I_9$ (A: methylammonium or cesium) for solar cell application. *Adv. Mater.* 27, 6806–6813,

[93] Lyu, M. Q., Yun, J. H., Cai, M. L., Jiao, Y. L., Bernhardt, P. V., Zhang, M., Wang, Q., Du, A. J., Wang, H. X., Liu, G., et al. (2016). Organic-inorganic bismuth (III)-based material: a lead-free, air-stable and solution-processable light-absorber beyond organolead perovskites. *Nano Res.* 9, 692–702,

[94] Zhang, X. Q., Wu, G., Gu, Z. W., Guo, B., Liu, W. Q., Yang, S. D., Ye, T., Chen, C., Tu, W. W., Chen, H. Z. (2016). Active-layer evolution and efficiency improvement of $(CH_3NH_3)_3Bi_2I_9$-based solar cell on TiO_2-deposited ITO substrate. *Nano Res.* 9, 2921–2930,

[95] Hoye, R. L. Z., Brandt, R. E., Osherov, A., Stevanović, V., Stranks, S. D., Wilson, M. W. B., Kim, H., Akey, A. J., Perkins, J. D., Kurchin, R. C., et al. (2016). Methylammonium bismuth iodide as a lead-free, stable hybrid organic-inorganic solar absorber. *Chem. Eur. J.* 22, 2605–2610,

[96] Hu, W. P., He, X., Fang, Z. M., Lian, W. T., Shang, Y. B., Li, X. C., Zhou, W. R., Zhang, M. M., Chen, T., Lu, Y. L., et al. (2020). Bulk heterojunction gifts bismuth-based lead-free perovskite solar cells with record efficiency. *Nano Energy* 68, 104362,

[97] Tong, T., Dou, X. Y., Zhang, H. R., Wang, H. X., Li, M., Hu, G. H., Wen, J. F., Jiang, L., et al. (2024). Enhancing the photocatalytic activity of lead-free halide perovskite $Cs_3Bi_2I_9$ by compositing with Ti_3C_2 MXene. *Molecules* 29, 5096,

[98] Saparov, B., Hong, F., Sun, J. P., Duan, H. S., Meng, W. W., Cameron, S., Hill, I. G., Yan, Y. F., Mitzi, D. B., et al. (2015). Thin-film preparation and characterization of $Cs_3Sb_2I_9$: a lead-free layered perovskite semiconductor. *Chem. Mater.* 27, 5622–5632,

[99] Kim, Y., Yang, Z. Y., Jain, A., Voznyy, O., Kim, G. H., Liu, M., Quan, L. N., de Arquer, F. P. G., Comin, R., Fan, J. Z., et al. (2016). Pure cubic-phase hybrid iodobismuthates $AgBi_2I_7$ for thin-film photovoltaics. *Angew. Chem. Int. Ed.* 55, 9586–9590,

[100] Zhou, J., Zhao, F., Shen, J. H., Zhou, Y., Wu, Y., Guo, Y. X., Jiang, J. C., Chu, J. H. (2021). Inorganic lead-free antimony-based perovskite-inspired solar cells with a carbon electrode and green anti-solvent regulation. *J. Mater. Chem. C* 9, 15301–15308,

[101] Xiao, Z. W., Du, K. Z., Meng, W. W., Wang, J. B., Mitzi, D. B., Yan, Y. F. (2017). Intrinsic instability of $Cs_2In(I)M(III)X_6$ (M = Bi, Sb; X = halogen) double perovskites: a combined density functional theory and experimental study. *J. Am. Chem. Soc.* 139, 6054–6057,

[102] Cheng, P.F., Zheng, D. Y., Feng, L., Liu, Y. F., Liu, J. X., Li, J. T., Yang, Y., Wang, G. X., Han, K. L. (2022). Doped all-inorganic cesium zirconium halide perovskites with high-efficiency and tunable emission. *J. Energy Chem.* 65, 600–604,

[103] Sakai, N., Haghighirad, A. A., Filip, M. R., Nayak, P. K., Nayak, S., Ramadan, A., Wang, Z. P., Giustino, F., Snaith, H. J. (2017). Solution-processed cesium hexabromopalladate(IV), Cs_2PdBr_6, for optoelectronic applications. *J. Am. Chem. Soc.* 139, 6030–6033,

[104] Qiu, X. F., Jiang, Y. N., Zhang, H. L., Qiu, Z. W., Yuan, S., Wang, P., Cao, B. Q. (2016). Lead-free mesoscopic Cs_2SnI_6 Perovskite solar cells using different nanostructured ZnO nanorods as electron transport layers. *Phys. Status Solidi Rapid Res. Lett.* 10, 587–591,

[105] Qiu, X. F., Cao, B. Q., Yuan, S., Chen, X. F., Qiu, Z. W., Jiang, Y. N., Ye, Q., Wang, H. Q., Zeng, H. B., Liu, J., et al. (2017). From unstable $CsSnI_3$ to air-stable Cs_2SnI_6: a lead-free perovskite solar cell light absorber with bandgap of 1.48 eV and high absorption coefficient. *Sol. Energy Mater. Sol. Cells* 159, 227–234,

[106] Lee, B., Krenselewski, A., Baik, S. I., Seidman, D. N., Chang, R. P. H. (2017). Solution processing of air-stable molecular semiconducting iodosalts, $Cs_2SnI_{6-x}Br_x$, for potential solar cell applications. *Sustainable Energy Fuels* 1, 710–724,

[107] Ghosh, B., Chakraborty, S., Wei, H., Guet, C., Li, S. Z., Mhaisalkar, S., Mathews, N. (2017). Poor photovoltaic performance of $Cs_3Bi_2I_9$: an insight through first-principles calculations. *J. Phys. Chem. C* 121, 17062–17067,

[108] Harikesh, P. C., Wu, B., Ghosh, B., John, R. A., Lie, S., Thirumal, K., Wong, L. H., Sum, T. C., Mhaisalkar, S., Mathews, N. (2018). Doping and switchable photovoltaic effect in lead-free perovskites enabled by metal cation transmutation. *Adv. Mater.* 30, 1802080,

[109] Zhou, Y. Q., Xu, J., Liu, J. B., Liu, B. X. (2021). Alloy engineering in mixed Sn-Ge perovskites for photovoltaic application. *J. Mater. Chem. A* 9, 6955–6961,

[110] Du, K. Z., Meng, W. W., Wang, X. M., Yan, Y. F., Mitzi, D. B. (2017). Bandgap engineering of lead-free double perovskite $Cs_2AgBiBr_6$ through trivalent metal alloying. *Angew. Chem. Int. Ed.* 56, 8158–8162,

[111] Greul, E., Petrus, M. L., Binek, A., Docampo, P., Bein, T. (2017). Highly stable, phase pure $Cs_2AgBiBr_6$ double perovskite thin films for optoelectronic applications. *J. Mater. Chem. A* 5, 19972–19981,

[112] Wu, C. C., Zhang, Q. H., Liu, Y., Luo, W., Guo, X., Huang, Z. R., Ting, H., Sun, W. H., Zhong, X. R., Wei, S. Y., et al. (2018). The dawn of lead-free perovskite solar cell: highly stable double perovskite $Cs_2AgBiBr_6$ film. *Adv. Sci.* 5, 1700759,

[113] Luo, T., Zhang, Y. L., Chang, X. M., Fang, J. J., Niu, T. Q., Lu, J., Fan, Y. Y., Ding, Z. C., Zhao, K., Liu, S. Z. (2020). Dual interfacial engineering for efficient $Cs_2AgBiBr_6$ based solar cells. *J. Energy Chem.* 53, 372–378,

[114] Zhang, Z. Y., Sun, Q. D., Lu, Y., Lu, F., Mu, X. L., Wei. S. H., Sui, M. L. (2022). Hydrogenated $Cs_2AgBiBr_6$ for significantly improved efficiency of lead-free inorganic double perovskite solar cell. *Nat. Commun.* 13, 3397,

[115] Ihtisham-ul-haq, Khan, M. I., Farhat, L. B., Elhouichet, H., Patil, R. P. (2025). Enhancing efficiency of $Cs_2AgBiBr_6$ double perovskite solar cells through bandgap reduction by molybdenum doping. *J. Korean Ceram. Soc.* 62, 359–369,